NOISE-TOLERANT WAVEFRONT SHAPING FOR FOCUSING LIGHT THROUGH MULTIMODE FIBERS

A THESIS SUBMITTED TO
THE GRADUATE SCHOOL OF ENGINEERING AND SCIENCE
OF BILKENT UNIVERSITY
IN PARTIAL FULFILLMENT OF THE REQUIREMENTS FOR
THE DEGREE OF
MASTER OF SCIENCE
IN
MATERIALS SCIENCE AND NANOTECHNOLOGY

By
Amna Ammar
July 2025

Noise-Tolerant Wavefront Shaping for Focusing Light through Multi-mode Fibers
By Amna Ammar
July 2025

We certify that we have read this thesis and that in our opinion it is fully adequate, in scope and in quality, as a thesis for the degree of Master of Science.

Hasan Yılmaz(Advisor)

Abdullah Demir

Ege Özgün

Approved for the Graduate School of Engineering and Science:

Orhan Arıkan
Director of the Graduate School

ABSTRACT

NOISE-TOLERANT WAVEFRONT SHAPING FOR FOCUSING LIGHT THROUGH MULTIMODE FIBERS

Amna Ammar
M.S. in MATERIALS SCIENCE AND NANOTECHNOLOGY
Advisor: Hasan Yılmaz
July 2025

Multimode optical fibers (MMFs) offer unique advantages for high-resolution imaging, optical communication, and power delivery. However, their complex modal structure poses significant challenges for the precise prediction of light propagation. This thesis explores the upper bounds of intensity enhancement achievable in light focusing through multimode fibers (MMFs) using phase-only wavefront shaping techniques designed to be robust against noise.

We begin with a theoretical analysis of modal propagation and introduce the transmission matrix (TM) formalism as a foundation for describing input-output field relationships in MMFs. We then explore digital optical phase conjugation (DOPC) and feedback-based wavefront shaping strategies, emphasizing their performance limitations under realistic experimental constraints.

A central contribution of this thesis is the introduction of a generalized expression for the enhancement factor, incorporating both the input participation ratio and the phase error coefficient. We demonstrate that enhancement is strongly influenced by the choice of input basis and the presence of experimental noise. Using common-path interferometric transmission matrix (TM) measurements, we demonstrate that the Dual Reference Algorithm (DRA) implemented in the Hadamard basis outperforms the widely used Stepwise Sequential Algorithm (SSA) operating in the canonical (SLM pixel) basis. Our experimental results confirm that Hadamard-based wavefront shaping offers superior noise resilience, yielding intensity enhancement factors approaching the theoretical upper bound.

We further conduct a detailed analysis of experimentally measured transmission matrices (TMs), revealing that the segment size on the SLM significantly

influences modal coupling and focusing performance.

Finally, we introduce an operator-based framework that encodes the radial memory effect for a focused beam, extending beyond the conventional rotational memory effect in multimode fibers (MMFs). This approach enables beam scanning via controlled shifts of the input SLM pattern, paving the way for advanced applications in fiber-optic imaging and beam steering.

Overall, this thesis presents a unified framework that bridges theory and experiment to optimize wavefront shaping in multimode fibers (MMFs), with direct implications for endoscopic imaging, clean-beam fiber amplification, and programmable fiber-based optical systems.

Keywords: Wavefront shaping, Multimode fiber, Transmission matrix, Spatial light modulator, Enhancement factor, Participation ratio, Phase error, canonical basis, Hadamard basis, Optical memory effect.

ÖZET

ÇOK MODLU FİBERLERDE IŞIK ODAKLAMA İÇİN GÜRÜLTÜYE DAYANIKLI DALGACEPHESİ ŞEKİLLENDİRME

Amna Ammar
Malzeme Bilimi ve Nanoteknoloji, Yüksek Lisans
Tez Danışmanı: Hasan Yılmaz
Temmuz 2025

Çok modlu optik fiberler (MMF'ler), yüksek çözünürlüklü görüntüleme, optik haberleşme ve güç iletimi gibi uygulamalarda benzersiz avantajlar sunar. Ancak, karmaşık mod yapıları nedeniyle ışığın bu fiberler içerisindeki yayılımını hassas biçimde öngörmek oldukça zordur. Bu tez, yalnızca faz kontrolüyle yapılan dalga cephe şekillendirme teknikleri kullanılarak MMF'ler üzerinden ışık odaklamada elde edilebilecek ışık şiddeti artırımının teorik üst sınırlarını, deneysel gürültüye karşı dayanıklı olacak şekilde araştırmaktadır.

Bu tezde ilk olarak, mod yayılımını teorik olarak analiz ediyor ve giriş-çıkış alan ilişkilerini tanımlamak için iletim matrisi (TM) formalizmini temel alıyoruz. Ardından, sayısal optik faz konjügasyonu (DOPC) ve geri-beslemeye dayalı dalga cephe şekillendirme stratejilerini inceliyor, bu tekniklerin gerçekçi deneysel koşullar altındaki performans sınırlamalarına odaklanıyoruz.

Bu tezin temel katkılarından biri, hem giriş katılım oranını hem de faz hata katsayısını içeren genelleştirilmiş bir ışık şiddeti artırım faktörü ifadesi sunmaktır. Artırımın, kullanılan giriş dalgalarının bazına ve deneysel gürültünün varlığına son derece duyarlı olduğunu gösteriyoruz. Ortak-yol interferometrik TM ölçümleri kullanarak, Hadamard tabanında çalışan Çift Referanslı Algoritma'nın (DRA), yaygın olarak kullanılan Adım Adım Sıralı Algoritma'ya (SSA) kıyasla daha yüksek performans sunduğunu ortaya koyuyoruz. Deneysel sonuçlarımız, Hadamard tabanlı dalga cephe şekillendirmenin daha güçlü gürültü dayanıklılığı sağladığını ve teorik üst sınıra yakın ışık şiddeti artırımları elde edilebildiğini doğrulamaktadır.

Ayrıca, deneysel olarak ölçülmüş iletim matrislerini ayrıntılı şekilde analiz ederek, SLM üzerindeki segment boyutunun, optik fiber mod bağlaşım verimi ve odaklama performansını ciddi ölçüde etkilediğini gösteriyoruz.

Son olarak, çok modlu fiberlerde (MMF'ler) odaklanmış ışığın radyal hafıza etkisini kodlayan ve geleneksel dönel bellek etkisinin ötesine geçen operatör tabanlı bir çerçeve sunuyoruz. Bu yaklaşım, girişteki SLM deseninin kontrollü kaydırılması yoluyla ışık huzmesinin taranmasına olanak tanıyarak, fiber optik görüntüleme ve ışın yönlendirme uygulamaları için yeni olanaklar açmaktadır.

Genel olarak, bu tez, çok modlu fiberlerde dalga cephe şekillendirmeyi optimize etmek üzere kuramsal ve deneysel yaklaşımları birleştiren bütüncül bir çerçeve sunmaktadır. Sonuçlar, endoskopik görüntüleme, temiz ışınlı fiber amplifikasyonu ve programlanabilir fiber tabanlı optik sistemler gibi alanlarda doğrudan uygulamalara sahiptir.

Anahtar sözcükler: Dalga cephesi şekillendirme, Çok modlu fiber, İletim matrisi, Artış faktörü, Yalnızca faz giriş modülasyonu, Katılım oranı, Giriş faz hataları, Kanonik bazda SSA algoritması, Hadamard bazında Dual Reference algoritması.

Acknowledgement

It feels only right to begin by thanking my PI, Asst. Prof. Hasan Yılmaz, as my love for optics began when I realized that, as an electrical engineer, I could explore this fascinating field of light. Learning optics was far from easy; I often felt lost, buried under equations and experiments I could not understand. But Hasan Hoca's guidance and constant encouragement helped me find my footing, reminding me that confusion is part of the process and that progress is built one small insight at a time. His support made every hard moment feel worth it, and writing this now feels bittersweet, as if this chapter is ending while I still have so much left to learn. But as they say, every end is a new beginning.

As I wrap up this journey, I would like to thank Asst. Prof. Abdullah Demir and Asst. Prof. Ege Özgün, for agreeing to be a part of my thesis jury. I'd also like to thank Assoc. Prof. Seymur Jahangirov for being a remarkably brilliant researcher while remaining so humble, and Dr. Ayça Arslan-Ergül for being not only a mentor but also a friend, even opening her home to me on more than one occasion. Their kindness and example have inspired me deeply. I would like to thank all the members of ECOS Lab for sharing this journey with me. I want to thank Feykun and Mert for laying the groundwork in the lab before I joined; so much of what I was able to do was built on their efforts. And Serhan, you're a real one—thanks for being a great lab mate (and for all the random laughs along the way).

I would also like to acknowledge Bilkent University and UNAM, and the TÜBİTAK ARDEB Project (122F311, "Statistical optics in optical fibers with thousands of modes and its imaging applications"), for providing financial support for this work.

I am beyond grateful for my friends who have become family here at Bilkent. Noha and Kader, my besties since the start, I truly can't imagine life without you: thank you for every late-night talk, laughter-filled study session, and for

always showing up when it mattered. Momil, my sister across the hall, you hold a special place in my heart; thank you for being my comfort on hard days, for all the little kindnesses, and for making our dorm feel like home. Zahra, I don't know how you managed to become like a sister in less than a year, but I'm so glad you did. Can't wait to see you in Europe soon. Mikael, I'm so thankful for the joy and warmth you bring into my life. Emine, thank you for grounding me; I will miss our tea breaks so much. And Sylvana, your lovely smile brightens every room you walk into.

Thank you all for making this journey brighter. To the uncles at Mozart, thank you for knowing my breakfast order and making the start of my day delicious. To the cats of Bilkent, thank you for being the best natural stress relievers.

I want to especially thank my Pakistani friends who've been there since the beginning. Fatima and Rameesha, thank you for sticking around, even when I was kind of insufferable during undergrad. Hira, what a lovely thing it's been to see our friendship grow with us over the past 11 years, and for always showing up when I'm home. Ajiya and Alina, thank you for the catch-ups and laughter every time I'm back.

And to the people who have been my very first support system—my family. Here's to my mother, Muneeza Javed, who showed me that we should never be afraid to love deeply, and to my father, Ammar Masood, who taught me that a good sense of humor goes a long way. To Moiz, who will always be my baby brother, no matter how much gym he does to build his muscles. And to Tortilla, who's in heaven right now—I hope you're getting all the treats you deserve.

I find myself loving all of you more with each day I spend away. And above all, I thank Allah for making all of this possible.

I hold every one of you close to my heart.

"It isn't what we say or think that defines us, but what we do."

— Jane Austen, *Sense and Sensibility*

Dedicated to Mama, Baba, Moiz, & Tortilla

Contents

List of Figures

Chapter 1

Introduction & Motivation

Multimode fibers (MMFs) play a pivotal role across a wide range of optical technologies, including high-resolution single-fiber endoscopy [1–8], optical manipulation [9, 10], short-distance high-bandwidth communication [11], laser-based material processing [12], spectroscopy [13–15], and high-power fiber amplification [16–22].

The ability of MMFs to support multiple spatial modes enables high-throughput data transmission and efficient energy delivery. However, this same multimodal nature introduces challenges: modal dispersion [23, 24], intermodal interference [25, 26], and sensitivity to external perturbations [27] can lead to severe distortions in the transmitted light field.

These limitations have motivated a growing interest in developing wavefront shaping methods for controlling light propagation through MMFs. Wavefront shaping counteracts the effects of modal interference by carefully tailoring the input field to achieve a desired intensity distribution at the output [28–39]. While this thesis focuses on MMFs, it is worth noting that similar wavefront shaping principles have been successfully applied to integrated multimode waveguides, where they enable reconfigurable beam steering and programmable photonic circuits for on-chip applications [40, 41].

At the core of most wavefront shaping techniques is the transmission matrix (TM) [9, 42–44], which describes the linear relationship between the input and output optical fields. By measuring the TM, one can determine the optimal input field necessary to achieve a specific output pattern [2, 9, 11, 44–47]. This principle underlies various experimental approaches for controlling light through MMFs, including digital optical phase conjugation (DOPC) within feedback-based shaping using a spatial light modulator (SLM) [3, 42, 48–54]. While traditional methods focus on modulating the incident field with liquid crystal-based SLMs or digital micromirror devices (DMDs), an alternative strategy modifies the TM itself by applying controlled perturbations along the fiber's length, offering an all-fiber solution [55]. In this dissertation, the effectiveness of SLM-based wavefront shaping methods is evaluated using the enhancement factor as a central metric, which quantifies the increase in intensity at the target location relative to the intensity at the same target position for an unshaped input wavefront [31, 42, 50, 56].

Building on these foundational concepts, the remainder of this chapter presents a comprehensive theoretical framework that underpins the experimental and numerical work discussed throughout this thesis. Section 1.1 provides an overview of the structure and modal characteristics of MMFs. Section 1.2 introduces the TM formalism and its essential role in describing light propagation through MMFs. Section 1.3 outlines various wavefront shaping strategies, along with their experimental realization using spatial light modulators (SLMs). Finally, section 1.4 discusses the intensity enhancement factor η and the theoretical limits to the maximum η achievable through phase-only wavefront shaping in MMFs.

1.1 Step-Index Multimode Fibers (MMFs)

Optical fibers have become essential in numerous technological applications. One of the most well-known uses is in high-speed intercontinental communication. Beyond that, optical fibers are increasingly being employed in short-haul data transmission, particularly in data centers where high bandwidth and low latency are critical. In these settings, different types of fibers are used depending on the

required performance, including single-mode and multimode fibers [11].

In recent years, multimode fibers (MMFs) have gained significant attention, particularly in emerging fields such as biomedical imaging. A prominent example is single-fiber endoscopic imaging [1–7, 57], where MMFs are used to deliver and collect light deep within biological tissue using only a single flexible strand. Research into controlling light through MMFs is enabling the development of compact, high-resolution imaging systems.

Another area of interest is in broad-area fiber lasers [16–21]. For high-power laser applications, fibers with large core diameters, often multimode, are used to increase gain and avoid nonlinear effects. However, controlling the spatial properties of light in such fibers remains a challenge, making wavefront shaping techniques especially valuable [58, 59]. More recently, multimode fibers have also been explored as platforms for implementing programmable linear quantum optical networks, offering a scalable and compact alternative for photonic quantum information processing [60].

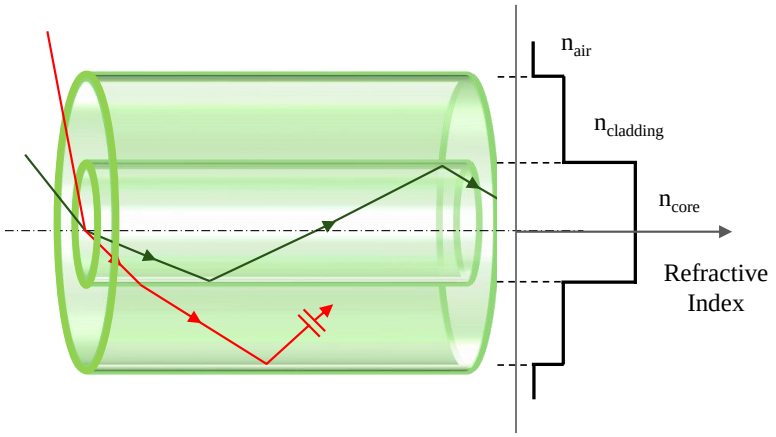

Figure 1.1: Illustration of a step-index multimode fiber showing the refractive index profile of the core, cladding, and surrounding air. Light is guided within the core through total internal reflection at the core–cladding interface.

To understand how light propagates in such systems, it is helpful to examine the structure of the fibers themselves. The fibers used in our experiments are step-index multimode fibers, as illustrated in Fig. 1.1. These consist of a core with a higher refractive index surrounded by a cladding with a slightly lower

index, guiding light via total internal reflection. The type of light propagation that occurs within such a fiber depends heavily on its modal structure.

To characterize the modal structure of a step-index fiber, we solve the scalar wave equation in cylindrical coordinates. Each guided mode corresponds to a solution with a unique propagation constant β, determined by matching boundary conditions at the core–cladding interface. This results in an equation involving Bessel functions that must be solved numerically to determine the allowed modes. In our numerical modeling of light propagation through MMFs, we adopt a mode decomposition approach, where the transmission matrix is constructed from the set of guided modes. Each column of this matrix represents a distinct mode [61], calculated based on the fiber's geometric and refractive index profile. Using the weakly-guiding approximation, the supported modes are treated as linearly polarized (LP) solutions to the scalar wave equation. To describe these modes mathematically, we define the radial components of the wavevector inside the core $h_a(x)$ and in the cladding $q_a(x)$, which are given by the following equations:

$$h_a(x) = a\sqrt{(n_{\text{core}}k_0)^2 - x^2}, \tag{1.1}$$

$$q_a(x) = a\sqrt{x^2 - (n_{\text{clad}}k_0)^2}, \tag{1.2}$$

where:

- a is the core radius of the fiber,
- n_{core} and n_{clad} denote the refractive indices of the core and cladding, respectively,
- $k_0 = 2\pi/\lambda$ is the wavenumber in vacuum,
- x is a potential propagation constant (β) value.

The propagation constants β of the supported LP modes are found by solving the transcendental equation:

$$h_a(x)\left(\frac{J_{l+1}(h_a(x))}{J_l(h_a(x))}\right) = q_a(x)\left(\frac{K_{l+1}(q_a(x))}{K_l(q_a(x))}\right), \tag{1.3}$$

where J_l is the Bessel function of the first kind (describing the field inside the core) and K_l is the modified Bessel function of the second kind (describing the field in the cladding), both of order l. This equation comes from matching the transverse field and its derivative at the core–cladding boundary and is solved numerically for each azimuthal index l to obtain the allowed discrete values of β.

Alternatively, full-vector modes can be calculated by solving the vector wave equation [61]. In our simulations, we use linearly polarized (LP) mode solutions of the vector wave equation, as polarization mixing is negligible in our experimental system, as confirmed in Chapter 2. Given that the propagation modes are treated as linearly polarized (LP) solutions, the focus is on a single polarization state for both the simulations and the experiment.

This polarization consideration becomes particularly important when comparing different types of optical fibers. In single-mode fibers, only the fundamental mode propagates, typically resembling a Gaussian-like profile. While these fibers are highly effective for long-distance transmission, they cannot transmit spatial patterns or images. On the other hand, multimode fibers (MMFs) support the simultaneous propagation of multiple transverse modes, each with its own distinct spatial profile and propagation constant. This increased modal capacity significantly enhances the fiber's capacity to carry more information, making MMFs ideal for applications requiring high data bandwidth.

This enhanced capability is due to the way the light propagates through these transverse modes. These modes are structured solutions of the wave equation that maintain their spatial profiles as they travel through the fiber [62–65]. When the fiber is excited with a single mode, the output field preserves the structure of that mode, but it is scaled by an amplitude and shifted in phase according to its propagation constant β. However, when an arbitrary input pattern, such as a star shape (as seen in Fig. 1.2), is launched into the fiber, it typically excites a superposition of multiple modes, resulting in a more complex output field.

This superposition leads to interference between the modes at the output, producing a seemingly random intensity distribution known as a speckle pattern.

The speckle pattern is spatially granular, with regions of high and low intensity due to constructive and destructive interference between the modes. While it may appear random, the speckle pattern is deterministic and encodes valuable information about the input field.

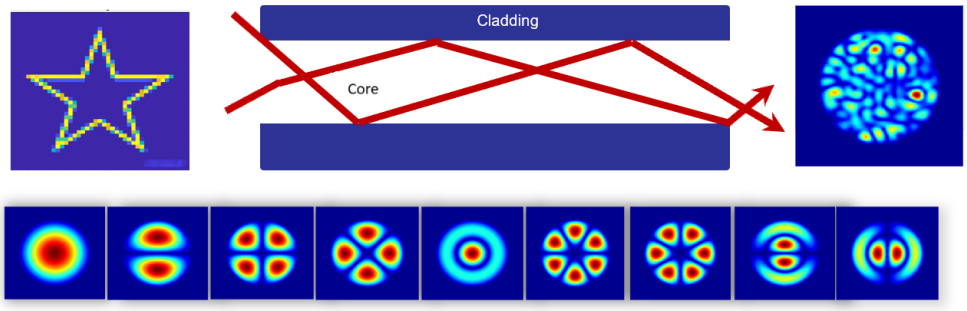

Figure 1.2: Light propagation through a step-index multimode fiber. A structured input field (left) excites multiple guided modes (bottom), which travel through the fiber at different velocities and interfere upon reaching the output. This modal interference produces a seemingly random speckle pattern (right).

The speckle formation illustrated in Fig. 1.2 can be described more formally as the coherent superposition of the fiber's guided modes. If the n^{th} mode is denoted by $\psi_n(x, y)$, then the total complex output field at the output takes the form:

$$E(x, y) = \sum_n a_n \psi_n(x, y) e^{i\beta_n L}. \tag{1.4}$$

Here, a_n denotes the excitation amplitude of the n^{th} mode (determined by input coupling), β_n is its propagation constant, and L is the fiber length. The observed intensity $|E(x, y)|^2$ is governed by both the relative amplitudes and the accumulated phase differences among modes. These phase terms encode the modal delays and are key to understanding the complex, yet deterministic, interference pattern observed at the output.

Physically, this accumulated phase arises because each guided mode travels at a different angle within the core, resulting in a unique longitudinal wavevector component and propagation constant β_n. The superposition of these phase-shifted

modes produces the intricate speckle field seen at the output.

Despite its seemingly random appearance, the speckle pattern is entirely deterministic. It reflects a fixed mapping between input and output fields, determined by the fiber's stable structure and the coherent nature of light propagation. In the absence of external perturbations [66], such as mechanical vibration, thermal drift, or other external perturbation sources, the same input field will always generate the same speckle pattern. There is no intrinsic randomness or phase decoherence in the system.

This inherent predictability naturally raises the question of controllability: if the input–output relationship is fixed, can one design an input field that produces a desired output pattern? In principle, the answer is yes. Because modal superposition is linear and each mode contributes a well-defined phase and amplitude, the input wavefront can be shaped to induce constructive interference at specific output locations. This concept forms the foundation of wavefront shaping, a technique that enables precise control over light propagation through complex or disordered media. The following section introduces this idea through the framework of the transmission matrix for a multimode fiber.

1.2 Transmission Matrix for MMFs

The transmission matrix (TM) offers a compact and quantitative framework for describing how input fields evolve as they propagate through a multimode fiber. It maps the complex input fields to the resulting output fields, fully characterizing the linear input–output behavior of the system.

In the ideal case of a short, straight MMF with no intermodal coupling and loss, the TM is unitary and diagonal: each input mode and its amplitude emerge unchanged at the output, apart from a mode-dependent phase shift determined by its propagation constant. This corresponds to a one-to-one mapping between input and output modes. In such a scenario, the TM's amplitude reduces to the

identity matrix, and predicting the output from a given input is straightforward.

In contrast, for longer fibers, on the order of several meters or more, imperfections such as bends, twists, or refractive index variations introduce significant coupling between modes [67]. As a result, light launched into a single input mode generally excites a superposition of modes at the output. This mode-mixing appears as non-zero off-diagonal elements in the TM. When expressed in the mode basis, the resulting matrix often appears statistically random [68–70]. Nonetheless, the system remains linear, and the underlying input-output relation still holds. Importantly, this linearity preserves time-reversal symmetry [71, 72], which enables the use of phase-conjugation techniques to refocus an output field back to its original input distribution.

To describe this input-output behavior more explicitly, we use the TM formalism '$E_{\text{out}} = tE_{\text{in}}$' where $E_{\text{in}} \in \mathbb{C}^N$ is the complex input field vector, $E_{\text{out}} \in \mathbb{C}^M$ is the output field vector, and $t \in \mathbb{C}^{M\times N}$ is the transmission matrix of the fiber as seen in Fig. 1.3. Each element t_{mn} describes the complex amplitude and phase coefficients from input segment n to output segment m. This relationship can be written more explicitly as:

$$\mathbf{E}_m^{(\text{out})} = \sum_{n=1}^{N} t_{mn}\mathbf{E}_n^{(\text{in})}. \tag{1.5}$$

The TM can be defined in any orthogonal basis, such as the basis of plane waves [73], the basis of guided modes [74], and the basis of foci [43], depending on the intended application.

While the TM fully characterizes the input-output field profile relationship through an MMF, it becomes practically useful only when it can be experimentally measured and used for wavefront control. One widely used method for doing so is digital optical phase conjugation (DOPC) [42, 43, 75, 76], which enables the reversal of light propagation through the fiber by reconstructing the phase-conjugated input field. The next section introduces DOPC as a core tool in feedback-based wavefront shaping methods.

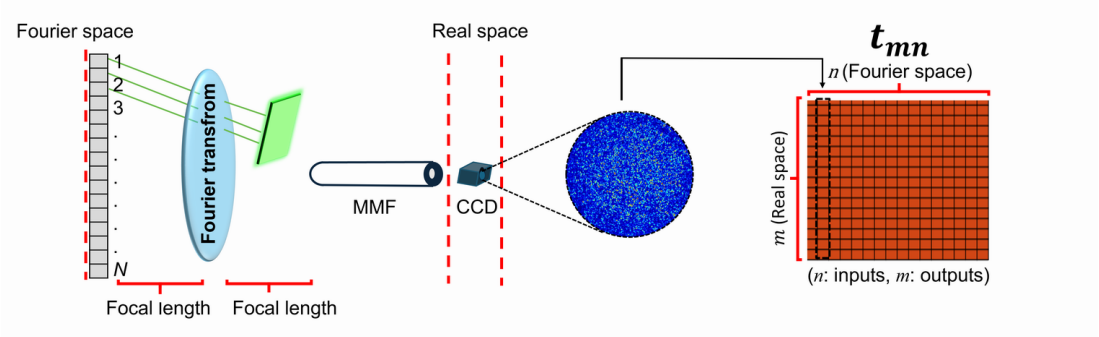

Figure 1.3: Transmission matrix (TM) acquisition through a multimode fiber (MMF). Each SLM pixel corresponds to a plane wave at a specific incident angle on the input facet of the fiber. The output field is measured on a CCD camera placed at the distal end. Each column of the TM corresponds to the complex output field distribution recorded when a single SLM pixel is addressed.

1.3 Digital Optical Phase Conjugation (DOPC) & Feedback - Based Wavefront Shaping

In our experiments, DOPC is used to generate the input wavefront that produces a diffraction-limited focus at a desired position at the fiber's output end. Unlike iterative methods that optimize over many input configurations, DOPC offers a direct solution once the TM has been measured. Focusing on arbitrary distal positions is achieved by selecting the corresponding row of the TM, which represents the output field response for all inputs at the desired focus point. For imaging applications, this focus is scanned sequentially across the field of view by using successive TM rows.

To clarify the structure of the TM in this context, each column represents the output field distribution resulting from a single input mode or SLM segment. Conversely, each row captures the field response at a specific output position. To focus light at the output position m at the distal end of the fiber, we use the complex conjugate of the corresponding row,

$$\mathbf{E}_n^{(\text{in})} = \sum_{m=1}^{M} t_{nm}^* \mathbf{E}_m^{(\text{out})}, \tag{1.6}$$

where t^* represents the complex conjugate of the transmission matrix, and $\mathbf{E}_m^{(\text{out})}$ corresponds to the desired field at the output. In case one wishes to focus light onto a single diffraction-limited spot—corresponding to the mth output channel—the desired output field $\mathbf{E}_m^{(\text{out})}$ is represented by a column vector of size $M \times 1$ containing a one at the mth position and zeros elsewhere:

$$\mathbf{E}_m^{(\text{out})} = \begin{bmatrix} \vdots \\ 0 \\ 1 \\ 0 \\ \vdots \end{bmatrix}. \tag{1.7}$$

This vector specifies that all energy is to be concentrated at the mth output channel, with no intensity at the others. When $\mathbf{E}_n^{(\text{in})}$ is displayed on the spatial light modulator (SLM), this input retraces the original propagation path in reverse, resulting in constructive interference at the target and forming a diffraction-limited focus.

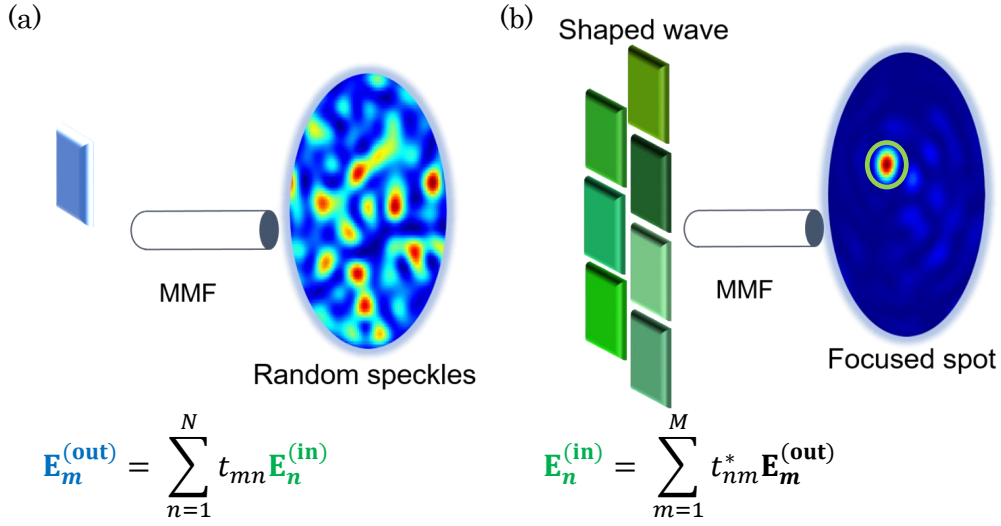

Figure 1.4: Schematic representation of speckle formation and wavefront shaping through a multimode fiber using digital optical phase conjugation is shown. (a) A random input wavefront produces a speckle pattern at the output. (b) Wavefront shaping with the conjugated transmission matrix phase produces a focused spot.

Experimentally, DOPC is implemented using a spatial light modulator

(SLM) [42] positioned at the fiber's proximal end. When a single segment on the SLM is activated, the resulting output appears as a speckle pattern, as described earlier. By scanning across all input segments and recording the corresponding complex output fields, typically using interferometric techniques [31, 43, 75, 77], the full TM can be measured. Once the TM is acquired, any desired output field can be reconstructed by applying the appropriate input composed of the linear superposition of the input segments. This is accomplished by programming the phase-only SLM with the corresponding phase profile. These SLMs, typically based on liquid crystal on silicon (LCoS) technology, allow precise pixel-wise phase modulation by electronically adjusting the voltage applied to each pixel.

However, measuring the complex output fields accurately presents several experimental challenges, especially in multimode fiber systems. Off-axis holography method uses a plane wave as a reference beam, which follows a different optical path than the signal beam's optical path. Therefore off-axis holographic method is highly sensitive to laser phase and frequency noise or environmental instabilities such as vibration and air currents [78]. Common-path interferometric method, in contrast, uses a portion of the signal as a reference that propagates along the same optical path, mitigating many of these instabilities [43]. In MMFs, however, this reference itself is a speckle pattern, requiring additional steps to isolate and subtract it. Structural perturbations, such as bending, twisting, or temperature fluctuations, can also dynamically alter the TM, complicating its measurement. In such scenarios, numerical modeling provides a practical alternative, enabling TM generation without relying on experimental stability [66, 79, 80]. Another approach is referenceless TM measurements, which use phase retrieval algorithms, but typically incur high computational costs [81].

Although this section has focused on DOPC in the context of multimode fibers, it is important to note that the technique was originally developed in the domain of disordered scattering media [3, 29, 42, 43, 75, 77, 82–84], where light propagation is highly random and diffusive. In such wavefront shaping experiments, performance is often quantified by the enhancement factor η, defined as the ratio of the optical intensity at the target position after wavefront shaping to the mean intensity at the same target position over random ensembles of many different

disorder realizations. In pioneering work [42], this metric was demonstrated to exceed 1,000, highlighting the remarkable focusing capabilities achievable even in strongly scattering environments.

1.4 Enhancement Factor

Building on the transmission matrix formalism and the concept of digital optical phase conjugation, we now turn to a central performance metric: the enhancement factor, η. It is formally defined as

$$\eta_m = \frac{I_m^{(\mathrm{foc})}}{\langle I_m^{(\mathrm{rand})} \rangle}, \tag{1.8}$$

where $I_m^{(\mathrm{foc})}$ is the intensity at the output position m after wavefront shaping, and $\langle I_m^{(\mathrm{rand})} \rangle$ is the mean intensity at the same position averaged over a large number of uncorrelated, random input wavefronts. This ratio captures the ability of wavefront shaping to direct and concentrate light energy at a desired spatial location, and serves as a quantitative benchmark for comparing different wavefront shaping strategies and system configurations [3, 31, 42]. The enhancement factor depends on several parameters, including the number of input degrees of freedom [53], the basis in which modulation is performed, and the level of experimental noise [85].

In practical implementations, wavefront optimization is typically carried out using algorithms that operate based on either feedback or a measured transmission matrix (TM) of the system [42, 86]. These algorithms aim to determine the ideal input field configuration that leads to constructive interference at the selected output location. In the ideal scenario where full control over both the amplitude and phase of all input channels is possible [53], the maximum enhancement factor corresponds to the number of input degrees of freedom, i.e.,

$$\eta = N. \tag{1.9}$$

However, in experimental systems, such complete control is rarely achievable.

Most spatial light modulators (SLMs), which are widely used for wavefront shaping, are limited to phase-only modulation [29]. Amplitude modulation is often avoided as it inherently reduces the total input power, making it inefficient for applications where high optical intensity is required. This includes scenarios such as high-power laser delivery, fiber amplifiers, and laser ablation through large-core MMFs [12, 20, 21, 87].

Under phase-only modulation, the achievable enhancement is fundamentally lower than in the full-field modulation case. The theoretical upper bound in this regime is given by

$$\eta = R(N-1) + 1, \tag{1.10}$$

where R is the participation ratio, a statistical measure of how many input channels effectively contribute to the interference at a given output point. For disordered scattering media, it is well established that $R = \pi/4$ under uniform random coupling conditions [31, 42, 56, 76, 85, 88]. However, the assumption that the participation ratio remains constant at $R = \pi/4$ in the context of MMFs has not been thoroughly scrutinized, prompting the question of whether MMFs exhibit similar statistical behavior to that of random media under phase-only modulation.

In this thesis, a comprehensive theoretical and experimental investigation is carried out to determine the upper bound of intensity enhancement achievable through phase-only wavefront shaping in MMFs. The study systematically explores how the participation ratio R depends on the choice of input basis used for phase modulation. Specifically, it is shown through both numerical simulations and experimental measurements that when the input modulation is performed in the Fourier basis, corresponding to placing the SLM in the Fourier plane of the fiber's proximal facet, the participation ratio remains constant at $R = \pi/4$ across the entire fiber output. This mirrors the behavior observed in disordered media, confirming that the theoretical bound remains applicable when modulation is performed in the Fourier basis. In contrast, modulation in the mode basis introduces a spatial dependence in R, due to the structured nature of the fiber modes.

To approach this upper bound in practice, this work adopts a noise-tolerant

wavefront shaping strategy based on Hadamard basis transmission matrix measurements. We also develop a predictive framework that incorporates phase error statistics into the expected enhancement, allowing us to quantify the gap between ideal and realistic focusing performance.

By linking theoretical predictions with experimental observations and explicitly modeling the effects of phase errors, this work establishes a robust framework for understanding and approaching the upper limits of phase-only wavefront shaping in MMFs. The findings hold direct relevance for high-resolution, ultra-thin endoscopes, optical communication, nonlinear fiber optics, and high-power laser delivery systems.

1.5 This Thesis

The chapters that follow introduce the physical and mathematical background of multimode fiber optics and wavefront shaping, describe the experimental and computational methods used for transmission matrix acquisition, analyze the role of phase errors and modulation basis on focusing performance, and conclude with an exploration of spatial memory effects using operator-based techniques.

Chapter 2 details the experimental procedure for transmission matrix (TM) acquisition and presents theoretical formulations for the enhancement factor η, with an emphasis on polarization mixing and the role of input participation ratio. Building on this, Chapter 3 quantifies the impact of phase noise and photon budget on η, comparing canonical and Hadamard modulation strategies. Extending beyond focusing, Chapter 4 explores the spatial memory effect in multimode fibers, introducing the radial-memory-encoded focusing operator that enables focusing with the radial memory effect. Finally, Chapter 5 summarizes key findings and discusses future research directions.

Chapter 2

Wavefront Shaping and Transmission Matrix in Multimode Fibers

Building on the foundational principles outlined earlier, this chapter introduces the theoretical and experimental framework of wavefront shaping to control light propagation through multimode fibers (MMFs). It begins with a detailed account of how the transmission matrix (TM) is experimentally measured. Key technical considerations, such as the basis in which the SLM is modulated (e.g, canonical pixel basis vs. Hadamard basis), the experimental geometry (e.g, placing the SLM in the Fourier plane), and polarization mixing, are critically examined as they fundamentally influence the measured transmission matrix, and ultimately the achievable enhancement factor in phase-only wavefront shaping.

2.1 Experimental TM measurement

Accurate measurement of the transmission matrix (TM) is essential for focusing light at specific positions at the distal end of a multimode fiber using digital

optical phase conjugation or other model-based wavefront shaping techniques. This section outlines the experimental setup, alignment procedure, and reflection-based validation techniques employed to ensure accurate and reproducible TM measurement for effective distal-end focusing.

The experimental setup used for TM measurement and wavefront shaping is illustrated in Fig. 2.1. A continuous-wave (CW) laser (Coherent OBIS LS, $\lambda = 561$ nm, 120 mW, fiber-coupled with FC connector) is collimated and linearly polarized in the horizontal direction using a half-wave plate (HWP) and polarizer (P). A beam splitter (BS) directs the horizontally polarized beam onto a reflective phase-only spatial light modulator (SLM; Meadowlark Optics, 1920×1152 pixels), which modulates the phase of the wavefront before coupling into the MMF.

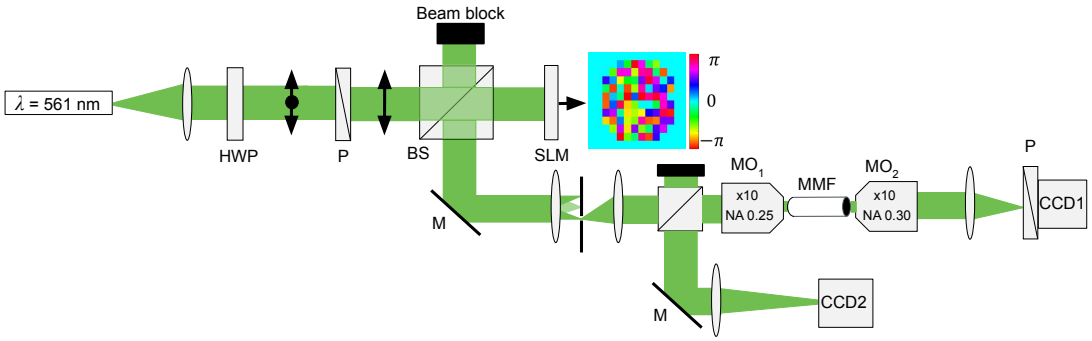

Figure 2.1: Schematic of the experimental setup for wavefront shaping through a multimode fiber (MMF). A linearly polarized beam at $\lambda = 561$ nm is modulated by a spatial light modulator (SLM) after polarization control using a half-wave plate (HWP) and polarizer (P). A blazed grating pattern is displayed on the SLM, and the modulated beam is filtered and focused into the proximal facet of the MMF using a 10× objective (MO_1). The output speckle is imaged using another 10× objective (MO_2) and recorded by CCD1, while CCD2 monitors back-reflection from the input facet.

The SLM provides a phase modulation range of 0 to 2π in discrete steps of $2\pi/160$, corresponding to the device's dynamic range. A binary phase grating with values $(0, \pi)$ and a period of 6 pixels is superimposed on the input patterns to suppress zeroth-order reflection and direct only modulated light into the first diffraction order. Each input pattern is composed of 6×6 pixel segments. For TM acquisition, a fixed random phase pattern is applied over these segments to

ensure uniform coupling across fiber modes, resulting in fully developed speckle at the output.

The modulated beam is reflected off the SLM, passes back through the BS, and is Fourier transformed by a lens ($f_1 = 150$ mm). A diaphragm in the Fourier plane blocks the residual unmodulated zeroth-order light. The beam is then relayed through a second lens ($f_2 = 150$ mm), Fourier transformed onto the back aperture of MO1, Fourier transformed, and coupled into the MMF (Olympus Plan 10×, NA = 0.25). The fiber is a 6-cm-long step-index MMF with a 200 µm core diameter and numerical aperture of 0.22, supporting approximately 15,178 modes per polarization at 561 nm.

The output pattern is imaged using another 10× objective (MO_2) and a lens, and recorded by CCD1, while CCD2 monitors back-reflection from the input facet at the proximal end. To ensure environmental stability during measurements, the setup is enclosed in a protective box and room temperature is maintained within ±1°C.

Maximizing the overlap between the modulated input field and the fiber's guided modes is crucial for efficient light coupling and accurate TM measurement. In real space, the input patterns must be centered on the fiber core, and their diameter must be less than or equal to the core size. In Fourier space, the angular spread of the input field must not exceed the fiber's numerical aperture, NA = 0.22. To ensure optimal coupling, we configured the SLM with 6×6 pixel-sized segments, resulting in a modulated field whose effective NA remained consistently below 0.22. This approach enabled near-perfect spatial and angular matching with the fiber's acceptance cone, ensuring efficient coupling of all modulated components.

To investigate the effect of different spatial phase modulations on the reflected intensity, we measured the back-reflection at the proximal end of the MMF under various input patterns applied to the SLM. The reflections in the top row of Fig. 2.2 exhibit bright, well-confined spots near the edge of the fiber core, signifying strong spatial overlap between the modulated input fields and the guided

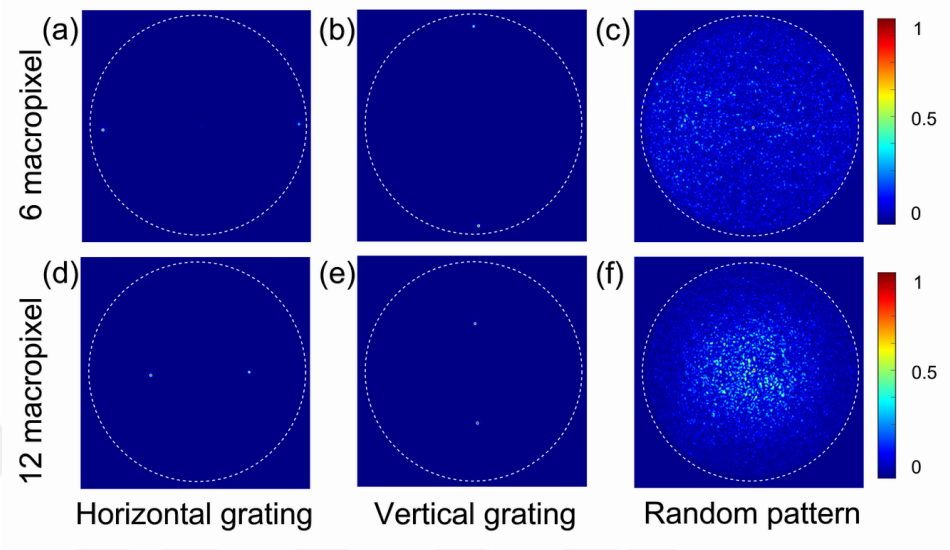

Figure 2.2: Experimental images of the reflected light intensity patterns at the proximal facet of the MMF. (a–c) Reflections for horizontal grating, vertical grating, and random phase patterns using 6×6 segments. (d–f) Corresponding reflection patterns for 12×12 segments. Confined reflection confirms proper alignment between SLM pattern and fiber core.

modes of the MMF. This confinement confirms that the chosen 6×6 segment resolution is well matched to the fiber core dimensions, ensuring effective angular and spatial coupling. In contrast, the bottom row of Fig. 2.2 (12×12 segments) shows coupled spots farther from the edge of the fiber core. This confinement suggests a mismatch between the coarser SLM segmentation and the fiber's core area. These observations highlight the importance of selecting an appropriate segment resolution to ensure optimal alignment between the SLM-modulated wavefront and the fiber's core. The confined reflections in the 6×6 case serve as an experimental validation of this spatial matching.

To enable unbiased comparison of intensity enhancement performance across bases, we maintained consistent output intensities by adjusting neutral density filters and verifying the mean intensity $\langle I \rangle$ under random inputs. So in all transmission matrix experiments, we recorded fiber output intensity images $I_m^{(\mathrm{rand})}$ corresponding to 1,000 random input wavefronts, using the same number of segments N as in each case. Figure 2.3 shows the mean transmitted intensity $\langle I \rangle$ recorded on CCD2 as a function of the number of controlled degrees of freedom N,

for both the canonical and Hadamard bases. Neutral density filters were adjusted throughout to ensure comparable intensity levels across all measurements.

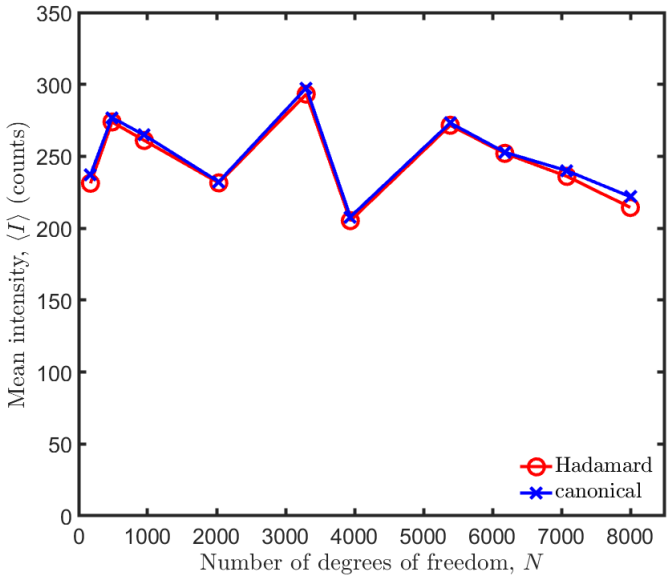

Figure 2.3: Mean intensity $\langle I \rangle$ recorded on the CCD camera as a function of the number of controlled degrees of freedom N in wavefront shaping experiments, measured using the Hadamard (red) and canonical (blue) bases. Neutral density (ND) filters were used during transmission matrix acquisition to maintain comparable intensity levels across both measurement bases.

After achieving precise alignment between the modulated input field and the MMF core and ensuring a comparable photon budget across our transmission matrix (TM) measurements, we proceed with the acquisition of the fiber's TM. Using the spatial light modulator (SLM) in our setup (Fig. 2.1), we select an input basis indexed by n, which can either be the canonical basis (where each SLM segment is independently addressed) or the Hadamard basis (where orthogonal superpositions of segments are used). The TM is measured using a common-path phase-shifting interferometry technique [15, 43, 89, 90], wherein the incident field is divided into a signal and a reference component, and the signal is modulated through four equally spaced phase steps between 0 and 2π. Both the signal and reference fields are then coupled into the MMF.

Having established the measurement method, we now describe the specific algorithms used. Depending on the choice of input basis, either the canonical basis

or the Hadamard basis, we employ two distinct retrieval strategies: the Stepwise Sequential Algorithm (SSA) and the Dual Reference Algorithm (DRA). The detailed principles and implementation steps for these TM acquisition methods are presented in the following section.

2.2 Transmission Matrix Acquisition Algorithms

One of the earliest and simplest approaches developed for wavefront shaping is a class of feedback-based optimization algorithms [56,76,85,86]. In these methods, a wavefront synthesizer—comprising a light source, spatial light modulator (SLM), and associated optics—iteratively adjusts the input field incident on a sample to maximize the output intensity, typically measured by a bucket detector or camera. A computer-executed control loop monitors the output and updates the input wavefront to converge toward an optimal configuration.

2.2.1 The Stepwise Sequential Algorithm (SSA) on the canonical basis

The first and most basic realization of this idea is the Stepwise Sequential Algorithm (SSA) [42]. Here, the SLM is divided into N segments, and four-phase shifting interferometry is performed individually on each segment. In each cycle, the relative phase between the selected segment and the remaining $N-1$ segments, acting as the reference signal, is swept from 0 to 2π. Repeating this process for all N segments enables the full reconstruction of the transmission matrix elements.

A main limitation of this approach is that the signal-to-noise ratio (SNR) deteriorates as the number of controlled degrees of freedom N increases [85]. This decline arises because the optical power contributed by a single segment becomes increasingly small relative to the combined reference field from the remaining segments.

During each optimization cycle, a single segment (highlighted in blue in Fig. 2.4) is selected and modulated while the other segments remain fixed. The phase of the modulated segment, denoted as ϕ_a, is varied continuously from 0 to 2π, and the corresponding target intensity I_b is recorded at each step.

The resulting intensity $I_b(\phi_a)$ can be expressed as:

$$I_b(\phi_a) = |E_{ba} + E_{b0}|^2 = |E_{ba}|^2 + |E_{b0}|^2 + 2\,|E_{ba}|\,|E_{b0}|\cos\left(\phi_{ba} + \phi_a\right), \tag{2.1}$$

where E_{ba} is the field contribution from the modulated segment, E_{b0} is the reference field from the unmodulated segments, and ϕ_{ba} denotes the intrinsic phase difference between the modulated field E_{ba} and the reference field E_{b0}.

Owing to the cosine dependence, the optimal phase ϕ_b^{opt} that maximizes I_b can be determined by measuring the output intensity at four phase steps—0, $\frac{\pi}{2}$, π, and $\frac{3\pi}{2}$—and applying the expression provided in Ref. [43];

$$\phi_{\text{opt}} = \tan^{-1}\left(\frac{I_b(\pi/2) - I_b(3\pi/2)}{I_b(0) - I_b(\pi)}\right). \tag{2.2}$$

Alternatively, one can perform a least-squares fitting [42, 76, 85], or use a general expression applicable when the number of sampled data points $I_b(\phi_a)$—corresponding to equally spaced phase values ϕ_a between 0 and 2π—is equal to or greater than three [91, 92], which is given by

$$\phi_{\text{opt}} = \tan^{-1}\left(\frac{\sum_{a=1}^{A} I_b(\phi_a)\sin(\phi_a)}{\sum_{a=1}^{A} I_b(\phi_a)\cos(\phi_a)}\right). \tag{2.3}$$

As the phase of a single segment is varied, its contribution interferes with the static field contributions from all other segments, resulting in a measurable change in the output intensity. By sequentially optimizing each segment in this manner, a fully optimized phase pattern can be constructed, enabling efficient coherent focusing onto the desired target position.

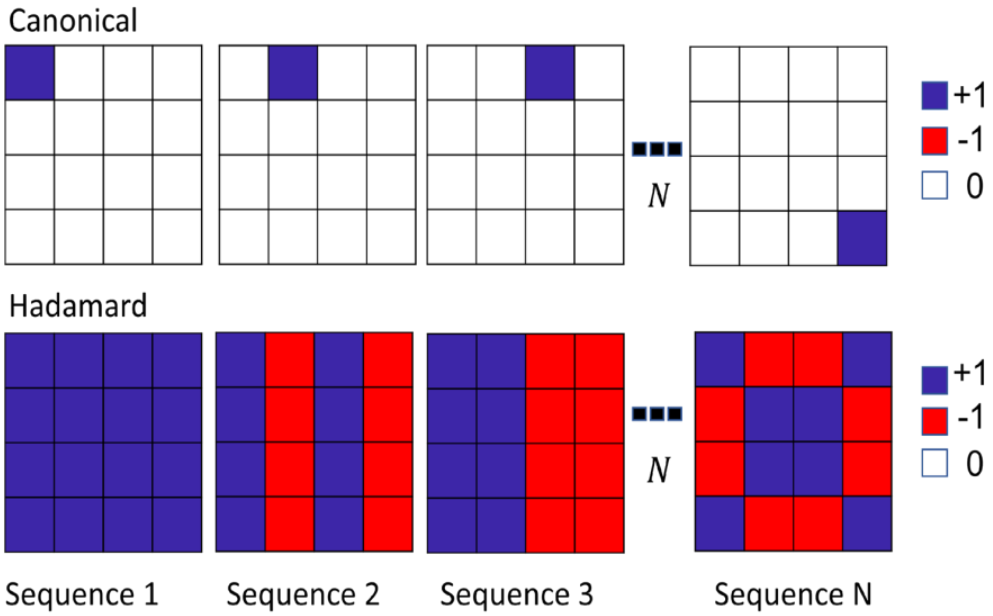

Figure 2.4: Comparison between the canonical (top) and Hadamard (bottom) bases used in wavefront shaping. The canonical basis modulates one segment at a time, while the Hadamard basis modulates many segments simultaneously using orthogonal patterns, improving signal-to-noise ratio in noisy conditions.

2.2.2 Dual Reference Algorithm (DRA) on the Hadamard Basis

To address the signal-to-noise ratio (SNR) limitations inherent in the Stepwise Sequential Algorithm (SSA), the Dual Reference Algorithm (DRA) adopts the Hadamard basis to enable simultaneous modulation of many segments. The Hadamard basis comprises a set of orthogonal binary patterns that are well-suited for implementation on phase-only spatial light modulators (SLMs). By modulating a large fraction of the input pixels in each pattern, this basis significantly enhances interferometric visibility at the output, leading to improved SNR during transmission matrix acquisition. Alternatively, this algorithm can be adapted to a different phase-only orthogonal basis set [93], instead of the Hadamard basis.

The Dual Reference Algorithm (DRA), introduced by Mastiani and Vellekoop [86], extends earlier Hadamard-based algorithms by integrating principles from both Popoff et al. [43] and Tao et al. [94]. In this approach, the spatial

light modulator (SLM) is divided into two equal groups of segments with a small overlapping region of size O. Each group is sequentially used as the modulated set while the other serves as a static reference. The overlapping region provides a stable phase reference, enabling the relative phase between the two measurements to be calibrated. This design allows the full complex transmission matrix to be reconstructed with greater resilience to noise.

The Hadamard basis is used for input modulation, and the total number of segments N must satisfy $N = 2^p$, where p is an integer (e.g., $N = 128, 256, 512, \dots$). In the first step of the algorithm, a Hadamard pattern is applied to Group 1 (segments 1 to N_1), while the remaining segments $N_1 + 1$ to N serve as a static reference field $E_{\text{ref}}^{(1)}$. Four-phase shifting interferometry is used to vary the relative phase between the modulated and reference fields across four values from 0 to 2π. The complex output field is then retrieved via a Hadamard transform on the full-field patterns, yielding a partial transmission matrix $t^{(1)}$ whose elements are relative to the $E_{\text{ref}}^{(1)}$ phase.

In the second step, the roles are reversed: Group 2 (segments $N-N_1+1$ to N) is modulated using the Hadamard basis, while Group 1 serves as the static reference field $E_{\text{ref}}^{(2)}$. Again, four-phase interferometry is applied to retrieve another partial transmission matrix $t^{(2)}$, this time relative to the $E_{\text{ref}}^{(2)}$ phase.

Because each group shares a subset of overlapping segments O, the phase difference between $E_{\text{ref}}^{(1)}$ and $E_{\text{ref}}^{(2)}$ at each camera pixel m can be calculated from the measured phase of the overlapping region in both steps. This relative phase offset is then used to adjust the phases of $t^{(1)}$ and $t^{(2)}$, and the final full-field transmission matrix is obtained by this phase correction. This correction enables seamless combination of the two measurements into a single, full-complex optimized wavefront.

Compared to SSA, DRA offers significantly improved signal-to-noise ratio, particularly in photon-budget-limited regimes, since a large fraction of the input segments are modulated simultaneously in each Hadamard pattern. Unlike Tao's pre-optimization scheme, DRA supports transmission matrix acquisition

alongside target-specific wavefront shaping, making it more flexible and scalable for advanced optical applications. A conceptual comparison between the canonical and Hadamard bases is shown in Fig. 2.4, illustrating the difference between segment-by-segment modulation and structured global modulation using orthogonal patterns.

2.3 Singular Value Decomposition (SVD) Analysis

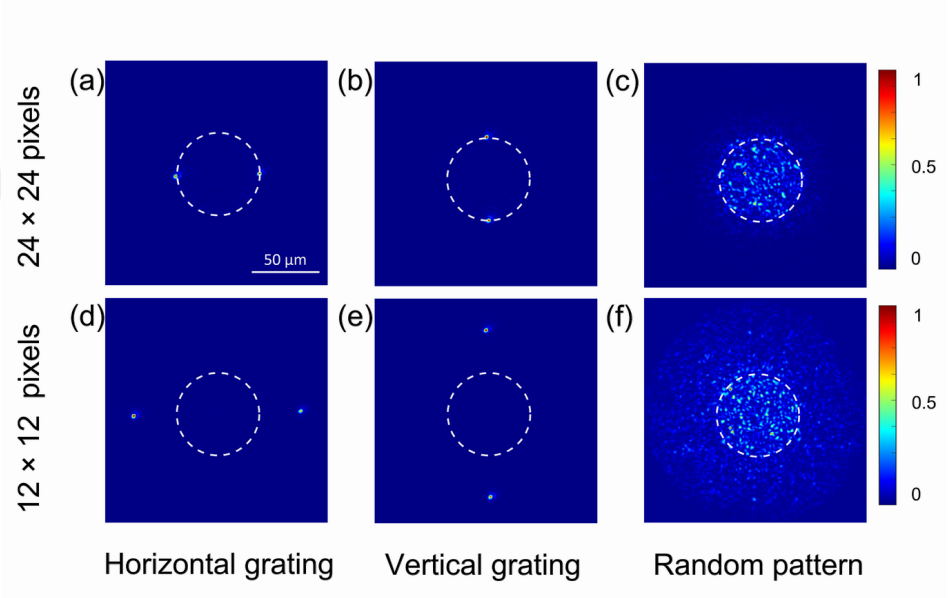

Figure 2.5: Reflected light intensity at the proximal end of a 50 µm core MMF for different phase patterns displayed on the SLM using 24×24 (top row) and 12×12 (bottom row) pixel-sized segments. (a,d) Horizontal grating, (b,e) vertical grating, (c,f) random phase pattern. The dashed circle indicates the fiber core.

To understand how light propagates through a multimode fiber (MMF), we performed a statistical analysis of the experimentally measured transmission matrix t, which maps complex input fields to output fields. A powerful way to study the structure of t is by applying the singular value decomposition (SVD) [95, 96]:

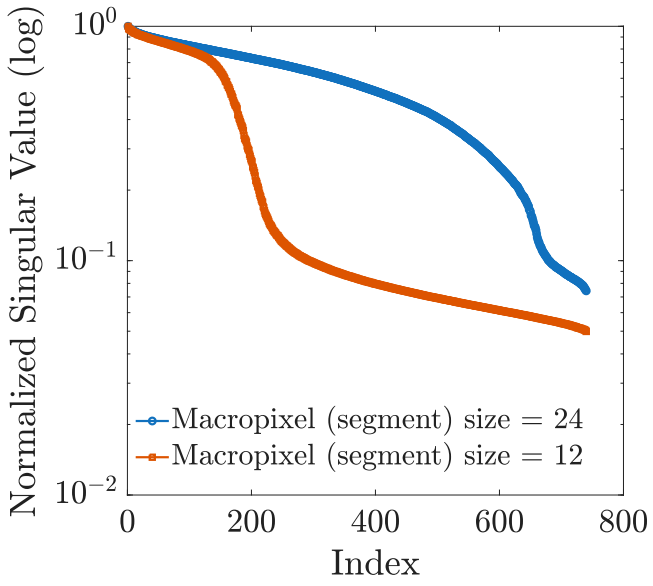

Figure 2.6: Normalized singular value spectra are shown for two TMs measured from a 50 µm core MMF at $\lambda = 561$ nm with $N = 740$ input segments. Results are shown for segment sizes of 12×12 pixels (red) and 24×24 (blue) pixels. The 24×24 segmentation yields a slower decay, indicating a relatively higher TM rank. In contrast, the 12×12 segmentation overfills the fiber core, causing rapid singular value decay and a reduction in effective TM rank.

$$t = U\Sigma V^{\dagger}. \tag{2.4}$$

Here, $V \in \mathbb{C}^{N\times N}$ is a unitary matrix whose columns are called the right singular vectors, representing orthonormal input patterns. $U \in \mathbb{C}^{M\times M}$ is another unitary matrix whose columns are the left singular vectors, representing output field patterns. The matrix $\Sigma \in \mathbb{R}^{M\times N}$ is diagonal and contains the singular values $\sigma_i \geq 0$, which quantify the transmission strength of each corresponding singular channel [97–100]. This decomposition provides insight into the modal content and effective degrees of freedom supported by the fiber system.

Before analyzing the singular values and vectors of the transmission matrix (TM), it is critical to ensure proper spatial coupling between the SLM patterns and the MMF core. To this end, we performed reflection measurements at the

proximal end of the fiber under different input modulations.

Fig. 2.5 shows the reflected intensity distributions for various phase patterns applied using 24×24 (top row) and 12×12 (bottom row) pixel-sized segments. When 24×24 segments are used, the modulated input beam remains well confined within the fiber core, leading to efficient coupling and minimal overfill. In contrast, the 12×12 case results in a larger modulated area, causing the input beam to exceed the fiber's proximal core diameter. This overfilling reduces coupling efficiency and introduces higher spatial frequencies, as evident from the broader angular distribution seen in the reflection patterns.

These differences in coupling behavior directly affect the structure of the measured TM, which we analyze using singular value decomposition (SVD). In an ideal case, if all the fiber modes transmitted light perfectly and equally, every singular value would be exactly 1 (assuming normalization). This would indicate that all input patterns are transmitted to the output with the same efficiency. In such a scenario, light can be delivered through any input mode without distortion or attenuation. However, in real experimental conditions, the singular values are not all equal. Instead, they exhibit a broad distribution, reflecting the unequal transmission efficiencies of different input-output mode pairs. Singular values close to one ($\sigma_i \approx 1$) indicate channels through which light is transmitted efficiently and coherently, while significantly smaller singular values ($\sigma_i \ll 1$) correspond to channels that are either poorly coupled, lossy, or dominated by experimental noise.

This uneven distribution arises from a combination of physical and technical limitations. First, mode-dependent losses in the multimode fiber can attenuate certain spatial modes more than others, reducing their contribution to the output field. Second, limited coupling efficiency, especially for high spatial frequency components, can result from the fiber's finite numerical aperture (NA), which restricts the range of angular components that can be injected or collected. Finally, measurement noise and phase retrieval errors, inherent to the process of transmission matrix acquisition (particularly in low-light (photon budget) or high-N

regimes), further distort the singular value spectrum, lowering the apparent transmission strength of some channels.

The singular vectors associated with large singular values define the most effective input wavefronts for delivering light through the fiber. We can optimize tasks like focusing, imaging, and beam delivery by targeting these high-transmission channels. Moreover, the number of significantly large singular values provides a measure of the system's effective degrees of freedom, i.e., how many independent modes meaningfully contribute to the transmitted light. This becomes crucial when assessing the limits of spatial resolution and enhancement in focusing experiments.

2.3.1 SVD of TMs from a 50-µm-diameter Core MMF

We performed SVD of a step-index MMF's two TMs with a segment size of 24×24 pixels and 12×12 pixels. The fiber has a length of about 6 cm, a core diameter of 50 µm, and a numerical aperture (NA) of 0.22. At an operating wavelength of $\lambda = 561\,\text{nm}$, the fiber supports approximately $1,000$ guided modes per polarization. Both TMs were acquired using $N = 740$ number of input degrees of freedom.

Fig. 2.6 shows the normalized singular value spectra for each case, plotted on a semilog scale. The singular value spectra show that the singular values drop at different rates with the channel index, indicating that the strength distribution of channels varies with segment size. For the 24×24 segment size, the singular values decay gradually, indicating efficient excitation of transmission channels.

In contrast, the TM measured with 12×12 pixel-sized segments exhibits a much steeper singular value decay. This finer segmentation overfills the fiber core at the proximal end, leading to lower coupling efficiencies. As a result, fewer input channels transmit significant power, leading to a reduced effective rank of the TM.

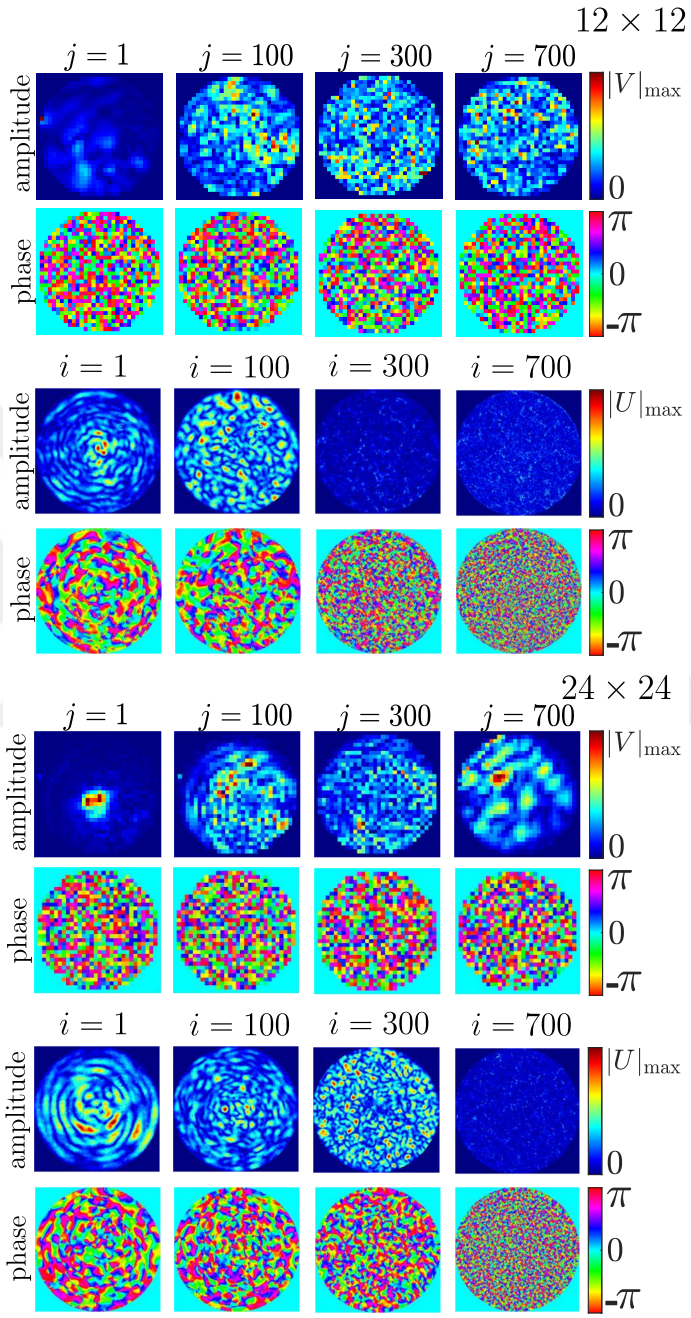

Figure 2.7: Representative left (U) and right (V) singular vectors obtained from the SVD of transmission matrices, expressed as $t = U\Sigma V^{\dagger}$. Results are shown for measurements with 12×12 (top) and 24×24 (bottom) SLM pixel-sized segments. Columns correspond to singular vector indices $i, j = 1$, 100, 300, and 700, with amplitude and phase shown.

We denote the singular vectors of the transmission matrix t as U_i and V_j, corresponding to the output and input channels, respectively. In Fig. 2.7, we display selected left (U) and right (V) singular vectors for representative indices $i, j = 1$, 100, 300, 700.

2.3.2 Comparison of Input Phase Structure and Focusing Across Segment Sizes

To investigate how the pixel segmentation affects spatial structure and focusing, we compared phase-conjugated input fields derived from transmission matrices measured using 12×12 and 24×24 pixel-sized SLM segments. Each configuration modulates $N = 740$ spatial input channels, arranged within a circular aperture of radius 16 pixels, corresponding to a 740-element input phase vector. For displaying on the SLM, these 740 values are mapped onto the active region by reshaping them into a circular phase mask and then expanding each segment using a Kronecker product with either a 12×12 or 24×24 pixel block, defining the physical phase modulation pattern.

Importantly, the input phase maps shown in Figures 2.8 and 2.9 correspond to the original un-kronned 740-element circular masks used to define the input phase vector, not the final segment-expanded SLM patterns. This ensures consistent visualization of spatial structure across segment sizes.

The output intensity distributions are computed on a 540×540 pixel grid, representing the full imaging area at the distal facet of the multimode fiber, whose core diameter also spans 540 pixels in this representation.

In the 24×24 case, the input phase maps are spatially smoother, leading to narrower ACFs and smaller full-width-at-half-maximum (FWHM) values. This indicates reduced spatial frequency content and a more confined angular spectrum, which better matches the fiber's numerical aperture and results in intense, sharply localized focusing.

Conversely, the 12×12 case input phase patterns exhibit finer spatial features, producing broader ACFs with larger FWHM values. This reflects higher spatial frequency content that extends beyond the fiber's acceptance cone, leading to overfilling and reduced coupling efficiency. The resulting focused spots are less intense and more diffuse.

These observations highlight that while smaller segments increase the number of controllable spatial degrees of freedom, this does not necessarily translate to better focusing. Instead, efficient modal coupling, enabled by proper angular matching between the modulated input field and the fiber modes, is essential for optimal performance.

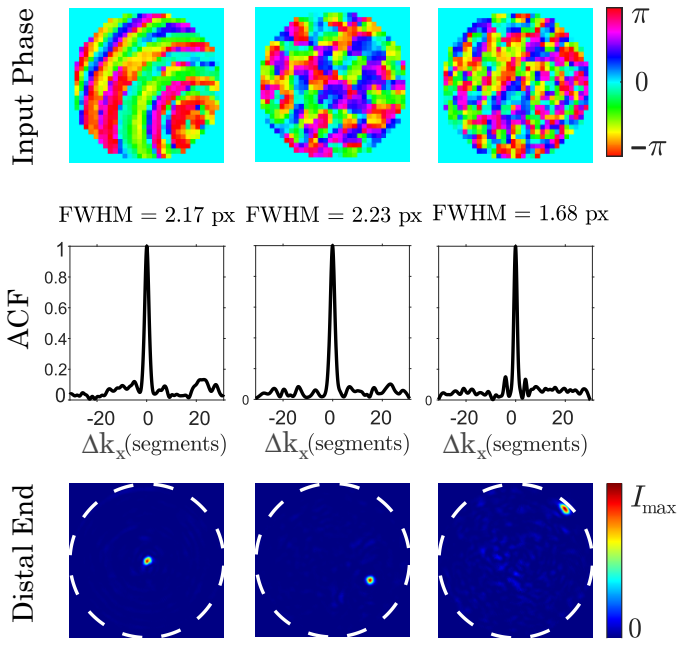

Figure 2.8: Spatial structure and focusing characteristics for phase-conjugated inputs computed using a TM measured with 12×12 pixel-sized SLM segments. Each column corresponds to a different target position. **Top:** Input phase patterns within the circular aperture. **Middle:** Autocorrelation functions (ACFs) of the input fields with corresponding full width at half maximum (FWHM) values. **Bottom:** Simulated focused intensity distributions at the fiber output facet.

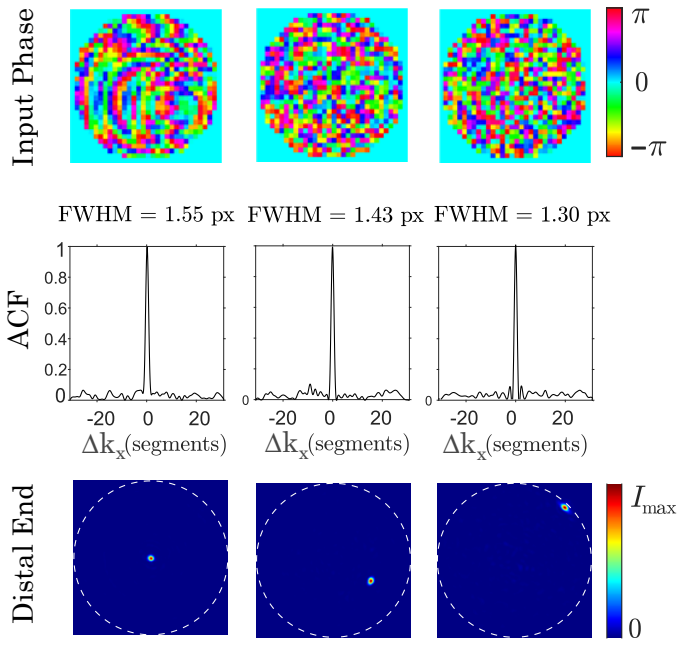

Figure 2.9: Spatial structure and focusing characteristics for phase-conjugated inputs computed using a TM measured with 24×24 pixel-sized SLM segments. Each column corresponds to a different target position. **Top:** Input phase patterns within the circular aperture. **Middle:** Autocorrelation functions (ACFs) of the input fields with corresponding full width at half maximum (FWHM) values. **Bottom:** Simulated focused intensity distributions at the fiber output facet.

2.3.3 Statistical Analysis of Focused Spot Profiles

To evaluate how segment size influences correlations between segments on the spatial light modulator, we analyzed the SLM phase profiles obtained by digital optical phase conjugation using experimentally measured transmission matrices (TMs) with 12×12 and 24×24 pixels per segment. In each case, the number of input degrees of freedom is $N = 740$. The input phase patterns on the SLM analyzed in this section have the unit of one segment, i.e., one phase value per data point, and the autocorrelation functions (ACFs) are computed over this domain. Therefore, the full width at half maximum (FWHM) values are reported in units of segments.

The left panel of Fig. 2.10 shows the azimuthally averaged full width at half

maximum (FWHM) of the autocorrelation function of the SLM field as a function of radial distance r of the focus position from the fiber core center. Each curve represents the mean FWHM over azimuthal positions at each radial distance, with error bars indicating the standard deviation. The dashed horizontal line shows the average FWHM obtained using random phase patterns, serving as a baseline for comparison. Across the radial range, the 24×24 segmentation consistently yields lower FWHM values than the 12×12 case, indicating the absence of correlation between the neighboring segments on the SLM. In contrast, the coarser 12×12 segmentation leads to broader FWHM values, indicating correlations between neighboring SLM segments. This correlation causes the input light to couple more strongly into the fiber core, as the resulting patterns with 12×12 segmentation typically exceed the core size in our setup.

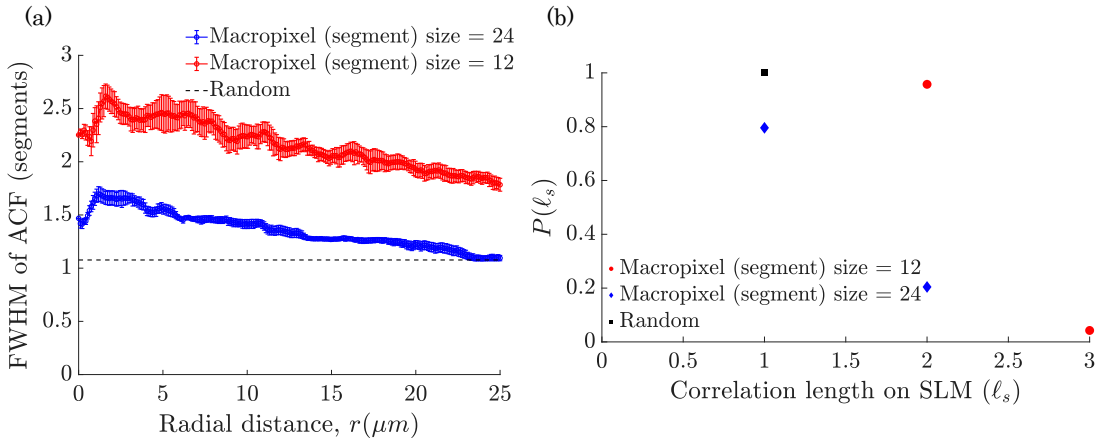

Figure 2.10: Statistical characterization of focusing performance using phase conjugation. a Azimuthally averaged full width at half maximum (FWHM) of the autocorrelation function of input phase maps, shown in units of segments: each representing a 12×12 (red) or 24×24 (blue) pixel block on the SLM. Error bars represent the standard deviation across focus realizations at the same radial distances. The dashed line shows the FWHM baseline for random input phases. Larger pixel-sized segments result in the absence of significant correlations among the neighboring segments.**b** Probability density functions (PDFs) of the correlation length on the SLM, ℓ_s. The random input (black) has the shortest ℓ_s due to fully uncorrelated phase values. The 24×24 segmentation (blue) yields intermediate correlation lengths, while the 12×12 case (red) produces the largest ℓ_s, reflecting smoother, longer-range phase variations.

The right panel displays the probability density functions (PDFs) of the correlation length ℓ_s on the SLM, extracted from the input phase patterns used for focusing. Shorter correlation lengths correspond to input fields with shorter range correlations between the neighboring segments, while longer ℓ_s indicate smoother, more slowly varying phase variations among the neighboring segments. As expected, the random input (black) exhibits the shortest correlation length. The input fields with 24×24 pixel-sized segments (blue) yield intermediate ℓ_s values, while the input fields with 12×12 pixel-sized segments (red) show the longest correlation lengths.

These results underscore a trade-off: although smaller segments allow finer control, they also introduce more high-angle components that fall outside the fiber's core. This leads to degraded input power coupling, as seen in the FWHM analysis. In contrast, larger segments yield input fields with sizes better matched to the fiber core size at the proximal end.

2.4 General Form of the Enhancement Factor (η) and its Theoretical Upper Limit

The enhancement factor, η, serves as a fundamental figure of merit in wavefront shaping experiments, characterizing the ability to concentrate light at a specific output position. It is defined as the ratio of the intensity at the optimized focal position to the average intensity at the same location under random input wavefronts. In the case of fully developed speckle patterns produced by scattering media, the theoretical upper bound for η under ideal phase-only modulation is given by [76]:

$$\eta_{\max} = \frac{\pi}{4}(N-1) + 1 \tag{2.5}$$

where N is the number of independently controlled input degrees of freedom. The prefactor $\pi/4$ arises from the statistical properties of interference in fully

developed speckle fields and will be discussed in the following section.

In practical settings, however, this ideal limit is seldom achieved due to experimental imperfections. One of the dominant factors limiting performance is phase errors [85] induced by experimental noise. A more realistic form of the enhancement factor that incorporates phase errors is:

$$\eta = \frac{\pi}{4}\left(\left|\sum_n \cos(\Delta\phi_n)\right|^2 - 1\right) + 1, \tag{2.6}$$

where $\Delta\phi_n$ denotes the phase error associated with input segment n. In the complex plane, the field contribution from each input segment can be represented as a phasor, i.e., a vector with fixed amplitude and controllable phase. When these phasors are perfectly aligned, they interfere constructively to produce a sharp focus. Phase errors introduce angular deviations, leading to destructive interference and lowering the output intensity. The cosine term quantifies this misalignment.

In recent work, Ammar et al. [101] developed a predictive framework for estimating phase errors prior to experimentation, providing new insights into how these errors scale with system parameters and measurement conditions.

To account for experimental non-idealities, we express the enhancement factor at the output pixel m as:

$$\eta_m = \alpha R_m \Phi_m (N-1) + 1, \tag{2.7}$$

where:

- $\alpha \equiv \langle A_n \rangle_n^2 / \langle A_n^2 \rangle_n$ captures the spatial homogeneity of the input amplitude profile,
- $R_m \equiv \langle |t_{mn}| \rangle_n^2 / \langle |t_{mn}|^2 \rangle_n$ is the participation ratio at the output pixel m,
- $\Phi_m \equiv \langle \cos(\delta\phi_{mn}) \rangle_n^2$ quantifies the degradation due to phase errors, $\delta\phi_{mn}$,

- N is the number of independently controlled SLM input segments.

In our experiments, the SLM is illuminated with a flat-top beam expanded from a single-mode fiber, ensuring $\alpha = 1$. The input index n corresponds to an SLM segment (in the Fourier plane), and the output index m corresponds to a pixel on the CCD camera at the fiber's distal end. The coefficient Φ_m captures how closely the measured phases of the transmission matrix match their true values. It ranges from $\Phi_m = 1$ in the absence of phase errors to $\Phi_m = 0$ under completely random phase noise. This term plays a central role in quantifying how phase errors degrade focusing performance.

It should be noted that the enhancement factor is not universally defined across the literature [53, 102]. In this work, we adopt a widely used convention [3, 31, 42, 50, 56, 75, 76, 85, 103], where the enhancement factor reaches a well-defined upper limit of $\eta = N_{\text{mode}}$ under ideal full-field (amplitude and phase) input modulation with $N = N_{\text{mode}}$, where N_{mode} denotes the total number of modes supported by a closed optical system, such as a multimode fiber.

To illustrate the impact of different wavefront shaping algorithms on enhancement, we present experimental results of two approaches. Figure 2.11 shows the output intensity distributions under three conditions: (a) a random input wavefront, (b) phase-only focusing using the Stepwise Sequential Algorithm (SSA) on the canonical basis, and (c) focusing using the Dual Reference Algorithm (DRA) on the Hadamard basis. In both focusing cases, the input fields were optimized to focus at the same radial and azimuthal positions (r, θ). The DRA produces a visibly stronger and more concentrated focus, owing to its higher accuracy in the transmission matrix measurement.

This figure illustrates the critical influence of both the input basis and the wavefront shaping algorithm on focusing performance. While localized focusing is achieved in both cases, the Dual Reference Algorithm (DRA) implemented in the Hadamard basis yields significantly higher peak intensity and better contrast. This improvement stems from its simultaneous modulation of multiple segments, which enhances interferometric visibility and reduces sensitivity to experimental

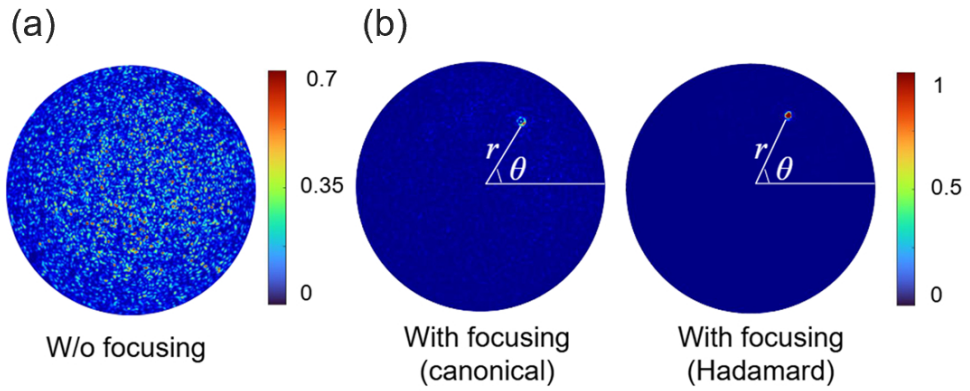

Figure 2.11: (a) Output speckle pattern at the distal end of the MMF resulting from a random input wavefront. (b) Focused intensity distributions obtained via wavefront shaping on two different bases: the canonical basis with the Stepwise Sequential Algorithm (left) and the Hadamard basis with the Dual Reference Algorithm (right). In both cases, the focus is directed to the same radial and azimuthal output positions (r, θ), marked by white guide lines. The Hadamard-based WFS method yields higher peak intensity and better contrast, reflecting improved noise resilience and phase accuracy.

noise in the intensity signal.

As shown in Eq. 2.7, the achievable enhancement is determined both by phase alignment (Φ_m) and by the effective number of input channels that contribute to the output, quantified by the participation ratio R_m. Our numerical calculations show that R_m is strongly influenced by the choice of input basis.

Building on these insights, the remainder of this chapter focuses on how the enhancement factor η depends on two key parameters: the participation ratio R_m and polarization mixing. The impact of phase errors, represented by $\delta\phi_{mn}$, will be addressed separately in Chapter 3.

2.5 Participation Ratio (R) Dependence of Enchancement Factor(η)

An important limitation in wavefront shaping arises when phase-only modulation is applied at the input, as is the case in many practical implementations. The participation ratio, denoted by R, captures the extent to which input degrees of freedom contribute to the output field. In phase-only modulation, R cannot reach unity because the spatial light modulator (SLM) controls only the phase and not the amplitude of the input field.

Despite this limitation, phase-only modulation is commonly used in high-power applications because it avoids the inherent power losses of amplitude modulation. When both phase and amplitude are controlled, many SLM pixels must be dimmed or turned off entirely, resulting in reduced power throughput. This is impractical for systems that require high optical power, such as fiber amplifiers, laser ablation setups, or nonlinear imaging techniques. In such cases, phase-only modulation offers a power-efficient alternative, and understanding the upper limit of performance achievable under this constraint becomes essential.

We determine R_m both numerically and experimentally. For the numerical analysis, we compute the transmission matrix using mode decomposition (see subsection 2.5.1) and apply a basis transformation to evaluate R_m in different input representations. Experimentally, we complement the phase measurements obtained from the dual-reference algorithm (Hadamard basis) by also measuring the amplitude contributions, which allows reconstruction of the full complex transmission matrix $t_{mn'}$. The matrix is then converted to the canonical (SLM pixel) basis using the Hadamard transform:

$$t_{mn} = \sum_{n'} t_{mn'} H_{n'n},$$

where $H_{n'n}$ is the unitary Hadamard matrix. Since phase-only modulation is implemented in the canonical basis, we compute the participation ratio in the

canonical basis.

Fig.2.12(a) illustrates the participation ratio R, obtained from both simulations and experiments, as a function of the normalized radial position r/a. When the spatial light modulator (SLM) is placed in the Fourier plane of the multimode fiber's (MMF) proximal end and phase-only input modulation is applied, the measured R remains nearly uniform across the fiber core at the distal end. This consistency holds for all focal positions and yields an average value of $R = \pi/4$, which is in close agreement with predictions from wavefront shaping studies in disordered media [88]. The strong agreement between simulation and experiment validates this behavior in the context of MMFs.

In our measurements, the fiber supports $N_{\text{mode}} = 15{,}178$ spatial modes per polarization, corresponding to a step-index profile with core radius $a = 100$ µm and numerical aperture NA = 0.22. To complement this, we also simulate light propagation through MMFs with core radii of $a = 15$ µm, 22 µm, 28 µm, and 38 µm, all using the same numerical aperture. These configurations result in respective mode counts of 180, 374, 606, and 1,114. All calculations assume a monochromatic wavelength of $\lambda = 561$ nm, matching the experimental conditions.

Although performing phase-only modulation directly in the fiber mode basis is not experimentally feasible, analyzing the participation ratio R in this representation provides important insight into the spatial structure of mode contributions at the output. Our numerical simulations show that when the modulation is conceptually performed in the mode basis, the value of R exhibits a strong dependence on the radial location of the target focus at the distal end of the MMF. In particular, near the center of the core, the participation ratio drops significantly, often below 0.2, due to the fact that most guided modes exhibit ring-shaped intensity distributions that carry little energy through the core center. In contrast, when the focal position is shifted toward the outer regions of the core, a larger number of modes contribute effectively, resulting in a higher R and improved focusing performance. Although not directly accessible in experiments, this basis-dependent behavior emphasizes the spatially inhomogeneous nature of modal structure in MMFs and further motivates the use of the Fourier basis,

where R remains uniform across the output plane.

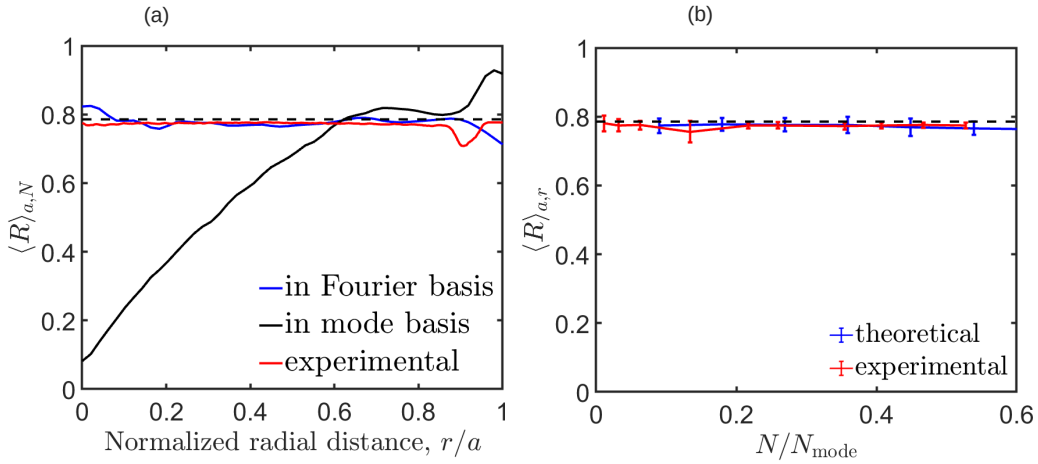

Figure 2.12: (a) The mean Participation Ratio R, averaged over the core radius a and the number of degrees of freedom N, versus the normalized radial distance r/a. The experimental R (solid red line) is consistent with the numerical R (solid blue line) in the Fourier basis, both following a trend close to $\pi/4$ (dashed black line) and showing no dependence on the radial distance. However, we observe a strong dependence of R on the radial distance when R is computed with phase-only modulation on the MMF fiber mode basis (solid black line). (b) The mean participation ratio R, averaged over the core radius a and the radial distance r at the fiber distal end, is shown with respect to the normalized number of degrees of freedom N/N_{mode}. The experimental R (red line) closely matches the numerical results (solid blue line) and remains invariant with N/N_{mode}, maintaining a value near $\pi/4$ (dashed black line). Here, $N_{\text{mode}} = 15,178$ for a fiber with $a = 100$ µm and NA $= 0.22$ in experiments and $N_{\text{mode}} = 180$, 374, 606, and 1,114 for fibers with $a = 15$ µm, 22 µm, 28 µm, and 38 µm and NA $= 0.22$ in simulations.

Fig. 2.12(b) presents the theoretical and experimental values of the radially averaged participation ratio R in the Fourier basis, plotted as a function of the normalized input number of degrees of freedom N/N_{mode}. Here, N_{mode} denotes the number of guided modes per polarization, which is calculated from the normalized frequency parameter $V = 2\pi a, \text{NA}/\lambda$. For our step-index fiber with a core radius of a $= 100$ µm, numerical aperture NA $= 0.22$, and input wavelength $\lambda = 561$ nm, this yields $N_{\text{mode}} = V^2/4 \approx 15{,}178$.

Across the full range of tested number of degrees of freedom N, both the experimental data and numerical simulations confirm that the average participation ratio remains at $R = \pi/4$, independent of N/N_{mode}. This consistent behavior

highlights a key feature of Fourier-basis phase-only modulation: the statistical contribution of input degrees of freedom remains uniformly distributed across output positions, irrespective of how many modes are present in the system.

Our theoretical analysis and supporting experiments confirm that the characteristic factor $\pi/4$, well-known from wavefront shaping through random scattering media, also governs the enhancement behavior in multimode fibers. This correspondence arises because each input degree of freedom in the Fourier basis effectively excites a random superposition of fiber modes. As a result, the resulting interference patterns at the output exhibit speckle statistics that closely mimic those produced in disordered systems.

This statistical equivalence explains why the average participation ratio R in the Fourier domain remains fixed at $\pi/4$, independent of spatial location or the number of modulated inputs. It also reinforces the importance of input basis selection: placing the SLM in the Fourier plane of the MMF's proximal facet ensures uniform coupling across the guided mode space, allowing the system to reach the theoretical upper bound for enhancement under phase-only control.

2.5.1 Numerical Simulations: Participation Ratio

To analyze the effective number of input segments contributing to each distal position on the fiber, we compute the participation ratio in both the mode and Fourier input bases. This analysis is based on the numerically constructed transmission matrix t, which maps the input field distribution to the output field at the distal end of the fiber.

We start by expressing the real-space transmission matrix from the input position s at the proximal end to the output position m at the distal end using the fiber's guided modes:

$$t_{ms} = \sum_{l,p} \psi_{ml,p}\, e^{i\beta_{l,p}L}\, \psi^{\dagger}_{sl,p}, \tag{2.8}$$

where $\psi_{ml,p}$ and $\psi_{sl,p}$ are the mode field profiles at positions m and s respectively,

$\beta_{l,p}$ is the propagation constant for the mode indexed by radial number l and azimuthal number p, and L is the fiber length.

Alternatively, when the input field is defined on the modal basis, the transmission matrix simplifies to:

$$t_{ml,p} = \psi_{ml,p}\, e^{i\beta_{l,p}L}. \tag{2.9}$$

We then compute the participation ratio R_m at the output position m in the modal basis as:

$$\langle R_{ml,p}\rangle_{l,p} = \frac{\langle |t_{ml,p}|\rangle_{l,p}^2}{\langle |t_{ml,p}|^2\rangle_{l,p}}. \tag{2.10}$$

To evaluate the participation ratio in the Fourier basis, we apply a discrete Fourier transform from the right. The transmission matrix in this basis is given by:

$$t_{mn} = \sum_s t_{ms}\, D^{\dagger}_{ns}, \tag{2.11}$$

where D_{ns} denotes the two-dimensional discrete Fourier transform matrix.

The corresponding participation ratio at the output position m in the Fourier basis is then calculated as:

$$\langle R_{mn}\rangle_n = \frac{\langle |t_{mn}|\rangle_n^2}{\langle |t_{mn}|^2\rangle_n}. \tag{2.12}$$

The participation ratio R_m quantifies how evenly the input segments contribute to a given output location. Higher values of R_m reflect more uniform input participation, which is essential for achieving high enhancement under phase-only wavefront shaping. While R_m captures the influence of the effective number of degrees of freedom, polarization effects also play a significant role. In the following section, we examine how polarization mixing impacts the enhancement factor.

2.6 Polarization Mixing Dependence of η

Polarization scrambling in multimode fibers (MMFs) poses a major limitation for polarization-sensitive applications. Due to mode mixing and birefringence, the output polarization state can be altered during propagation. However, by carefully shaping the input wavefront, it is possible to suppress polarization mixing and retain control over the polarization channel [104, 105].

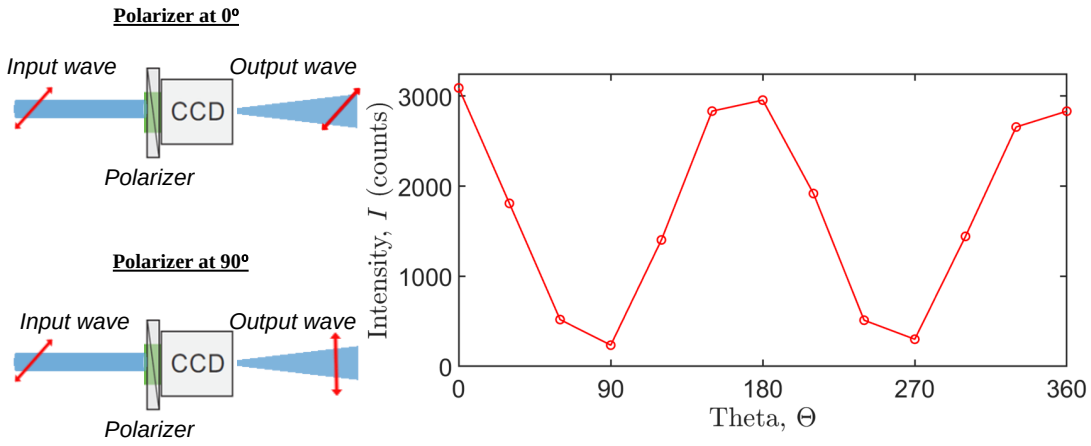

Figure 2.13: Schematic of polarization mixing measurement. (Left) Experimental setup with the output polarizer oriented at $\Theta = 0°$ and $90°$. (Right) Measured intensity as a function of rotation angle Θ, showing sinusoidal variation indicative of well-preserved linear polarization and minimal cross-polarization mixing.

To assess the level of linear polarization preservation in our setup, we place linear polarizers at both the input and output ends of the fiber. The output polarizer is rotated in discrete angular steps, and the resulting transmitted intensity is recorded using a CCD camera. As shown in Fig. 2.13, the intensity follows a clear sinusoidal dependence on the rotation angle Θ, with maxima at $\Theta = 0°, 180°$ and minima at $\Theta = 90°, 270°$. This confirms that the transmitted light retains its original polarization to a high degree and that cross-polarization components are strongly suppressed.

To further understand the impact of polarization mixing on the focusing performance, we simulate the mean enhancement factor η as a function of fiber length for two cases: one where only a single polarization is detected at the output, and

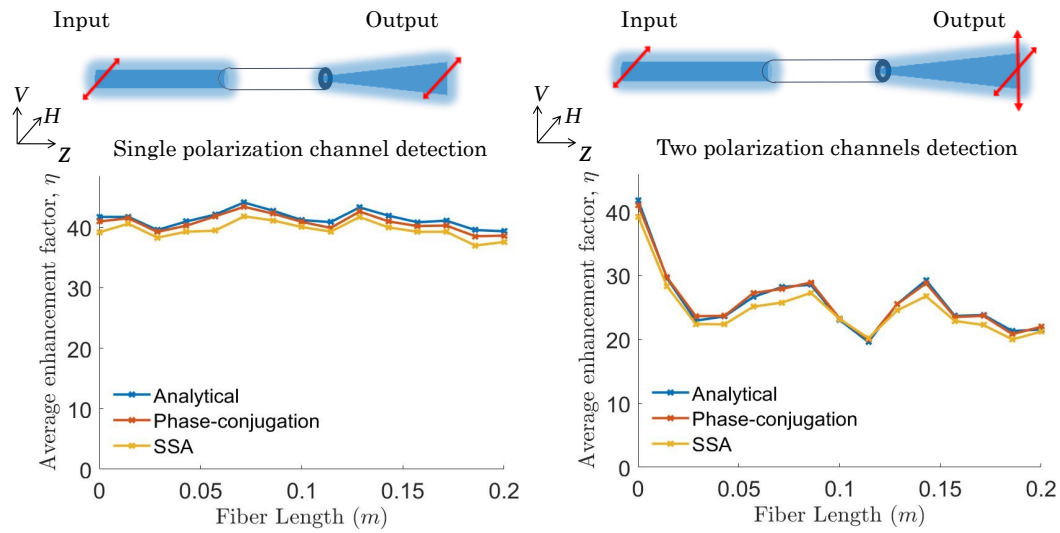

Figure 2.14: Enhancement factor η versus fiber length for systems with a single linear polarization detection and with both linear polarization detections at the output. The simulation considers 80 total guided modes (40 horizontal + 40 vertical) and 52 Fourier input modes. The presence of polarization mixing leads to a noticeable reduction in enhancement when both linear polarizations are detected at the output.

another where the intensity at both polarization states is detected. The system includes 80 total modes (40 horizontally and 40 vertically polarized) and 52 input degrees of freedom in the Fourier basis.

As shown in Fig. 2.14, the enhancement factor remains high and relatively constant across fiber lengths when only a single linear polarization is detected. In contrast, when both polarization channels are open, the enhancement drops significantly as the fiber length increases, due to increased mode mixing. This degradation highlights the importance of minimizing polarization mixing to achieve optimal focusing performance.

Chapter 3

The Effect of Phase Errors on Enhancement Factor η

In ideal wavefront shaping, one assumes perfect knowledge of the transmission matrix (TM) and precise control over the input field. However, real-world implementations inevitably suffer from experimental imperfections, particularly in the phase of the modulated input field. These phase errors, arising from noise [76, 89] expecially at low signal levels, directly degrade the quality of focusing through multimode fibers (MMFs).

As shown in the previous chapter, the enhancement factor η is highly sensitive to how well the input phases align to produce constructive interference at the target location. In phase-only modulation experiments, any deviation from the ideal phase profile reduces this constructive interference, limiting the achievable enhancement. This chapter focuses on quantifying the impact of such input phase errors on η. We present a combined theoretical and experimental analysis, introduce a statistical model to describe phase fluctuations, and validate the model through repeated TM measurements using different modulation bases.

3.1 Noise and Phase Error Dependence of η

In this section, we present a predictive methodology to quantify phase errors in transmission matrix measurements. We utilize phase-shift interferometry by taking two independent measurements for the same input pattern on the spatial light modulator (SLM). Ideally, in the absence of noise, the measured phases $\phi^{(1)}mn$ and $\phi^{(2)}mn$ for each input n and corresponding output m should be identical. However, due to experimental noise, phase errors $\delta\phi^{(1)}_{mn}$ and $\delta\phi^{(2)}_{mn}$ occur in both measurements.

To determine the phase errors, we define them as:

$$\delta\phi'_{mn} = \arg\left(e^{i(\phi^{(2)}_{mn} - \phi^{(1)}_{mn})}\right) \tag{3.1}$$

where $\phi^{(1)}_{mn}$ and $\phi^{(2)}_{mn}$ represent two independent measurements of the same input phase pattern, as can be seen in the illustration in Fig. 3.1. To statistically analyze these errors, we generate histograms of $\delta\phi'_{mn}$ and fit them with `MATLAB`'s `gauss1` function, which models the distribution as:

$$P(\delta\phi'_{mn}) = a\exp\left(-\left(\frac{\delta\phi'_{mn} - \mu}{\sigma_{\delta\phi}}\right)^2\right) \tag{3.2}$$

where $\sigma_{\delta\phi}$ denotes the standard deviation of the phase error distribution, and μ is its mean. The Gaussian fit allows us to extract $\sigma_{\delta\phi}$, providing a quantitative measure of phase fluctuations. Next, we numerically generate rescaled Gaussian-distributed random phase values ϕ_{mn} with mean $\mu = 0$ and standard deviation $\sigma_{\delta\phi}/\sqrt{2}$. Using these rescaled random phase errors, we compute the phase error coefficient:

$$\Phi_m \equiv \langle\cos(\phi_{mn})\rangle^2_n \tag{3.3}$$

where the averaging is performed over all inputs n. This coefficient quantifies how input phase errors impact the enhancement factor η.

Fig. 3.1(b) shows the standard deviation $\sigma_{\delta\phi'}$ of the fitted Gaussian functions

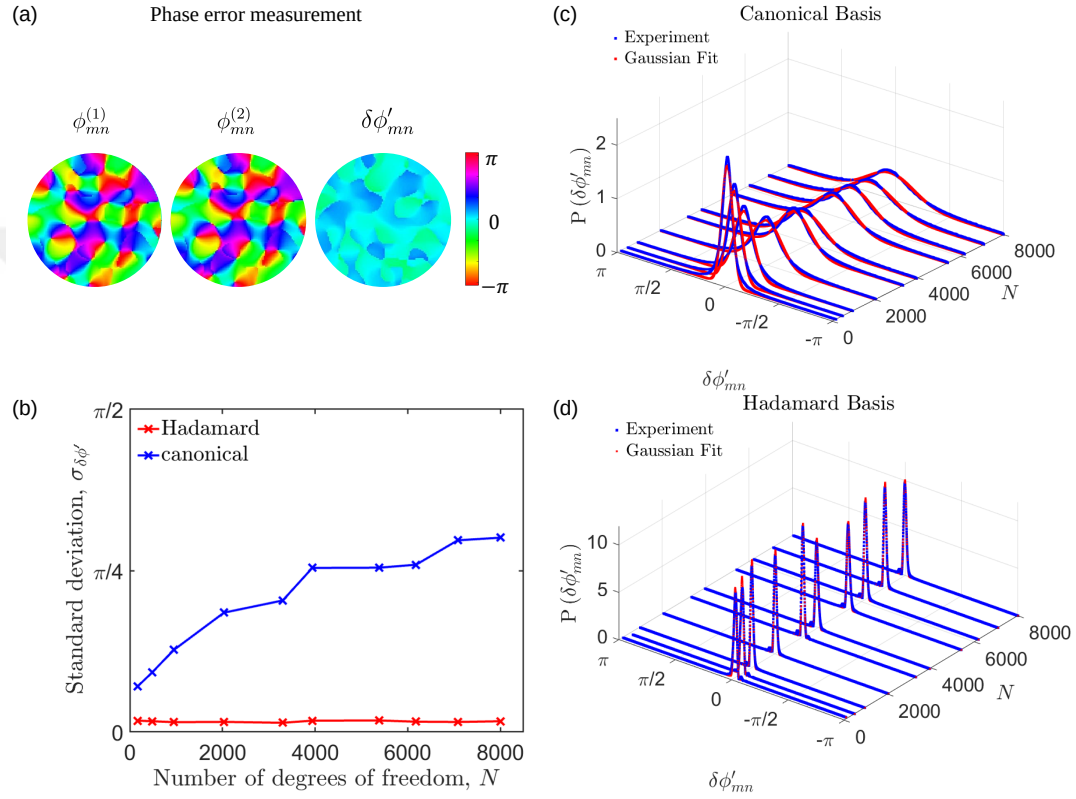

Figure 3.1: Analysis of phase errors in wavefront shaping experiments. (a) Visualization of two independently measured phase maps, $\phi^{(1)}_{mn}$ and $\phi^{(2)}_{mn}$, corresponding to the same input n and output m. The phase difference, $\delta\phi'_{mn} = \arg\left(e^{i(\phi^{(2)}_{mn} - \phi^{(1)}_{mn})}\right)$, represents the measured phase error. (b) Standard deviation $\sigma_{\delta\phi}$ of the Gaussian-fitted phase error distributions plotted as a function of the number of degrees of freedom N. In the canonical basis, $\sigma_{\delta\phi}$ increases with N, indicating a rise in phase errors. In contrast, the Hadamard basis maintains a consistently low $\sigma_{\delta\phi}$, suggesting better resistance to phase errors. (c) Probability density function $P(\delta\phi'_{mn})$ of the phase errors for the canonical basis, as a function of N, with Gaussian fits (red). The distribution widens as N increases, showing increasing phase errors. (d) Probability density function $P(\delta\phi'_{mn})$ for the Hadamard basis, also as a function of N. Here, the distribution remains sharply peaked around zero, demonstrating minimal phase errors and a robust performance even as N increases.

for phase error histograms obtained from different values of the number of degrees of freedom N. In the Hadamard basis, we observe that $\sigma_{\delta\phi'}$ remains consistently low across all measurements, suggesting that phase errors are minimal and well-controlled. On the other hand, in the canonical basis, $\sigma_{\delta\phi'}$ increases as N grows, indicating that phase errors become more pronounced with increasing input degrees of freedom, leading to broader phase error distributions. This trend highlights that as N increases, the quality of phase retrieval in the canonical basis deteriorates, resulting in greater deviations from ideal constructive interference.

3.2 Probability Densities of Phase Errors

It is important to understand the underlying statistical behavior of these errors in different wavefront shaping bases. The phase error distributions provide crucial insights into how noise manifests in each case and can influence the precision of phase retrieval. As we explore the phase error characteristics, we focus on the standard deviations of the phase errors in both the canonical and Hadamard bases.

As depicted in Fig. 3.2, significant differences are observed in the phase error standard deviations between the canonical and Hadamard bases. The phase error distribution in the Hadamard basis is narrower and more concentrated, indicating lower phase errors compared to the canonical basis. Fig. 3.2(a) shows the standard deviation $\sigma_{\delta\phi'}$ of the phase errors as a function of the normalized photon budget. In the canonical basis, phase errors are consistently higher across all photon budgets, with a particularly noticeable increase under low-light conditions where measurement noise becomes more significant. In contrast, the Hadamard basis demonstrates much lower phase errors, highlighting its robustness in maintaining precise phase retrieval even under reduced photon budgets. These findings underscore the importance of basis selection in minimizing phase errors, offering valuable insights for optimizing wavefront shaping performance in photon-budget-limited environments.

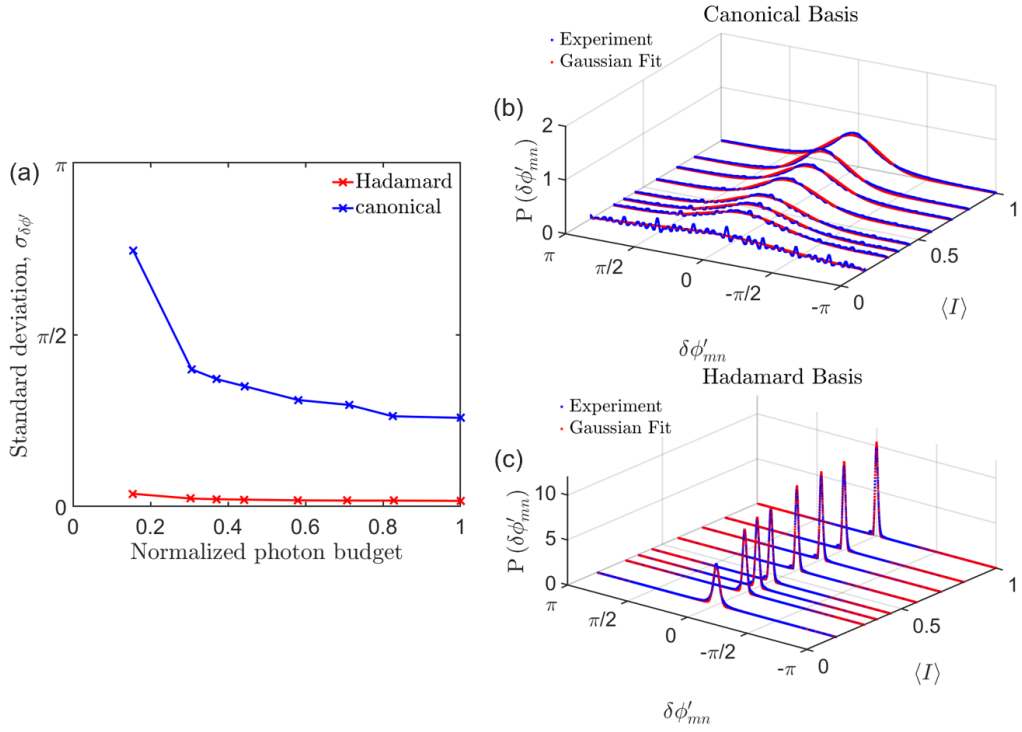

Figure 3.2: (a) Standard deviation $\sigma_{\delta\phi'}$ of the phase errors as a function of the normalized photon budget, comparing phase measurements in the canonical and Hadamard bases. The canonical basis shows significantly larger phase errors, especially at lower photon budgets, in contrast to the Hadamard basis. (b) and (c) Probability density functions of phase errors for the canonical and Hadamard bases, respectively. The blue curves represent the experimentally measured phase error distributions, while the red curves correspond to the Gaussian fits used to estimate the standard deviation $\sigma_{\delta\phi'}$. The phase error $\delta\phi'_{mn}$ is calculated as the difference between two independently retrieved output phase maps when the same input phase pattern is displayed on the spatial light modulator (SLM) once. The Gaussian fit provides the standard deviation $\sigma_{\delta\phi'}$, which quantifies phase fluctuations across different number of input degrees of freedom N. The standard deviations of phase errors are reduced by a factor of $\sqrt{2}$ to obtain ϕ_{mn}.

3.3 Phase Errors at Maximum Photon Budget

Wavefront shaping depends on achieving precise constructive interference at the target position, m, which makes it highly sensitive to phase errors introduced by experimental noise. To assess the degree of constructive interference in our experiments, we define the phase error coefficient Φ_m, given by:

$$\Phi_m \equiv \langle \cos(\delta\phi_{mn}) \rangle_n^2$$

At the target position, $\Phi_m = 1$ in the absence of phase errors, and approaches $\Phi_m = 0$ when phase errors render the measurements unreliable. Fig. 3.3(a) shows how phase deviations, $\delta\phi_{mn}$, disrupt the alignment of the field contributions, thereby decreasing Φ_m. In an ideal wavefront shaping experiment, the phases of all field contributions align perfectly, leading to strong constructive interference and high intensity at the target position. In practice, small phase errors cause slight misalignments of field contributions, resulting in Φ_m values close to 1.

These phase errors are inherently related to the mean photon budget during the TM measurements. The mean photon budget is defined as the mean number of detected photoelectrons recorded per measurement, averaged over the CCD camera pixels for a single input pattern. A higher mean photon budget ensures a better signal-to-noise ratio and more accurate phase retrieval, which is especially important in interferometric methods. In canonical basis measurements, for instance, Φ_m tends to be significantly lower, especially as the number of degrees of freedom, N, increases, due to more substantial phase errors.

To quantify the impact of accumulated phase errors, we experimentally determined the phase error coefficient, Φ_m, at each output position, and computed its ensemble average $\langle \Phi_{mn} \rangle_n$ as a function of N, as shown in Fig. 3.3(b). In the Hadamard basis, Φ_m remains close to 1, while in the canonical basis, it decreases significantly with increasing N. This degradation occurs because Hadamard-based wavefront shaping maintains a high signal-to-noise ratio by balancing the

signal and reference fields, ensuring maximum interferometric visibility. In contrast, for canonical basis measurements, as N increases, the signal strength diminishes, reducing the signal-to-noise ratio, which in turn degrades the interferometric contrast and limits the accuracy of the transmission matrix measurement.

To further investigate the effect of photon budget on phase errors, we analyzed Φ_m for a fixed $N = 8000$ as a function of the incident power on the CCD camera, as depicted in Fig.3.3(c). The photon budget was adjusted using neutral density (ND) filters placed in front of the CCD. For the Hadamard basis, Φ_m remains close to 1 even under reduced photon budgets, demonstrating its robustness in photon-budget-limited conditions [106]. This stability is due to the dual reference method's ability to preserve high interferometric contrast and a balanced signal-to-reference ratio, ensuring reliable phase retrieval. In contrast, for the canonical basis, Φ_m steadily decreases as the photon budget diminishes. This decline results from a reduced signal-to-noise ratio, leading to increased phase errors. As expected, when the photon count approaches zero, the accuracy of the phase error coefficient estimation degrades for both bases, eventually hindering the phase retrieval process.

3.4 Experimental η as a Function of r and θ

The theoretical participation ratio R remains constant across all output positions when using phase-only modulation in the Fourier (Hadamard) basis. Here we show that the experimental enhancement factor η exhibits a near uniform dependence on the radial distance at the distal end of the fiber.

Figure 3.4 shows the measured enhancement factor η as a function of radial distance r from the fiber core center for various values of the number of input degrees of freedom N. The results are presented for both the canonical basis using the Stepwise Sequential Algorithm (SSA) and the Hadamard basis using the Dual Reference Algorithm.

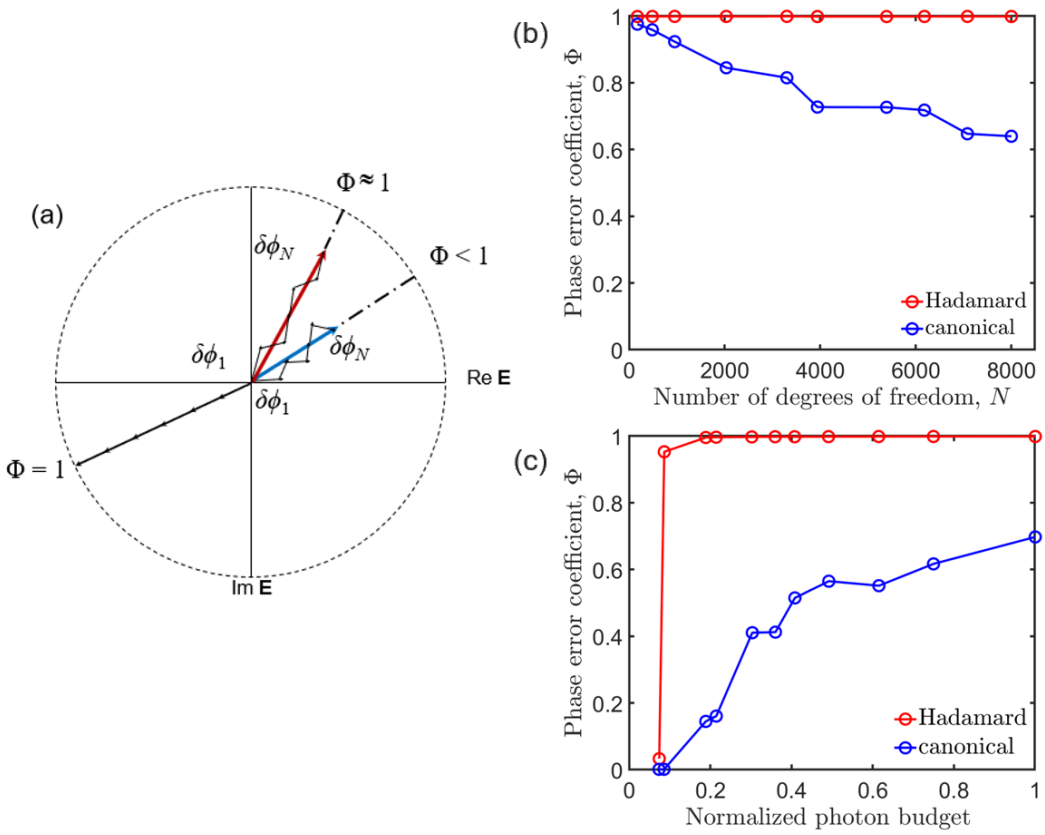

Figure 3.3: Effect of phase errors on the enhancement factor. (a) Schematic representation of the phase error coefficient Φ for the Hadamard (red) and canonical (blue) bases, where $\delta\phi$ represents phase errors. The dashed lines illustrate how phase errors accumulate differently in each basis, with the Hadamard basis maintaining $\Phi \approx 1$ due to a reduced cumulative effect of phase errors. (b) Variation of the phase error coefficient Φ with respect to the number of degrees of freedom N. In the canonical basis, Φ decreases as N increases due to a degradation in the signal-to-noise ratio (SNR), which results in lower interferometric visibility. In contrast, the Hadamard basis preserves a stable Φ, owing to its balanced signal-to-background ratio. (c) Plot of the phase error coefficient Φ for $N = 8000$ as a function of the normalized photon budget. The Hadamard basis consistently maintains a higher Φ compared to the canonical basis, indicating superior SNR under the same noise conditions. The normalized photon budget (ranging from 0 to 1) is defined such that the maximum corresponds to approximately 214 detected mean photoelectron counts.

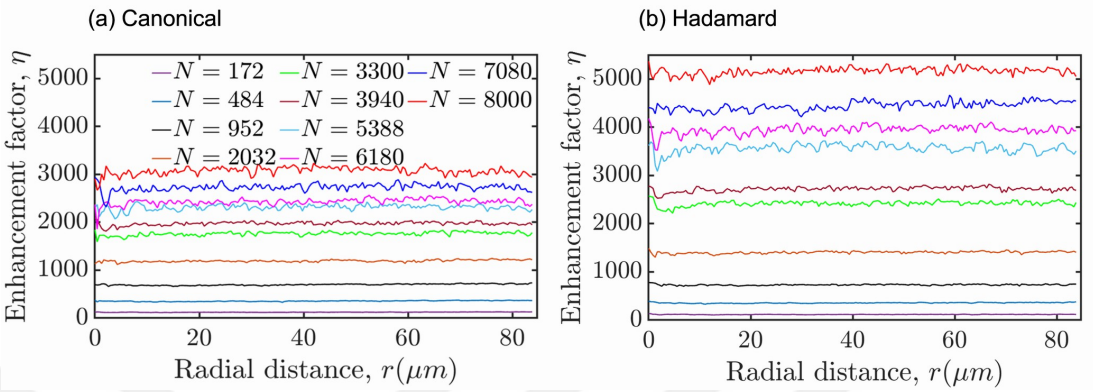

Figure 3.4: Enhancement factor η as a function of radial distance r at the fiber's distal end for various numbers of degrees of freedom N. **(a)** Canonical basis using the Stepwise Sequential Algorithm (SSA). **(b)** Hadamard basis using the Dual Reference Algorithm. Despite an equal theoretical participation ratio $R = \pi/4$, SSA exhibits reduced enhancement at larger r, especially for higher N, due to increased phase errors and reduced signal-to-noise ratio.

Notably, the Hadamard basis produces higher enhancement factors across the entire core, whereas the SSA results display more pronounced degradation, particularly at higher N. Since the participation ratio is constant in both cases, this discrepancy is attributed to the phase errors, which are more severe in SSA due to the reduced signal-to-noise ratio. These findings reinforce the conclusion that algorithmic robustness to phase noise is a dominant factor in determining the effective focusing performance.

To quantitatively evaluate the role of phase errors in shaping the enhancement factor η, we compare the experimental values with theoretical predictions under both full-field and phase-only modulation assumptions. Figure 3.5 presents the enhancement factor as a function of normalized radial distance r/a for four scenarios: ideal full-field control $\eta_{\text{full theor}} = N$, ideal phase-only control $\eta_{\text{phase theor}} = \frac{\pi}{4}(N-1)+1$, and experimental measurements for both Hadamard and canonical bases.

While the theoretical curves remain flat across the radial coordinate, the experimental values diverge from their respective upper bounds. Notably, the Hadamard-based enhancement closely follows the phase-only theoretical limit,

indicating minimal phase error accumulation. In contrast, the canonical basis results in a significantly lower η, confirming that phase errors dominate the discrepancy. These observations provide strong evidence that algorithmic robustness to phase noise is the key factor governing effective focusing performance, even when the participation ratio remains constant.

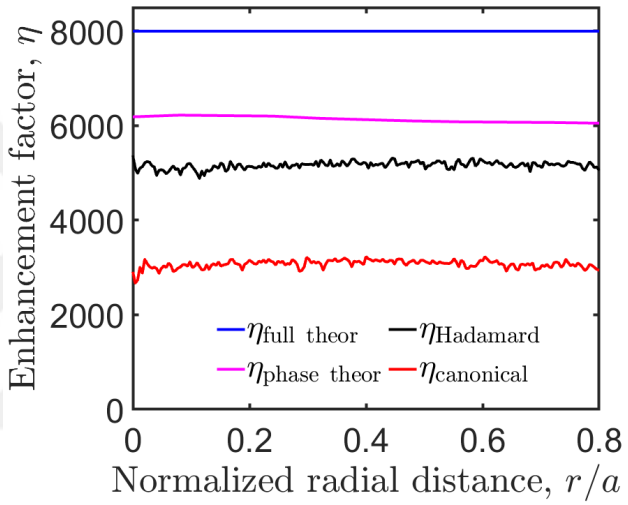

Figure 3.5: Enhancement factor η versus normalized radial distance r/a for theoretical and experimental cases. The full-field theoretical limit $\eta_{\text{full theor}} = N$ (blue) and the phase-only limit $\eta_{\text{phase theor}} = \frac{\pi}{4}(N-1)+1$ (magenta) serve as benchmarks. Experimental results using the Hadamard basis (black) approach the phase-only theoretical limit, while the canonical basis (red) underperforms significantly due to increased phase errors. This demonstrates that the effective limitation on η arises from phase error accumulation, not from participation ratio or spatial coupling efficiency.

Fig. 3.6 illustrates how the enhancement factor η, averaged over both radial (r) and azimuthal (θ) positions at the fiber output, evolves as a function of the number of controlled degrees of freedom N. When the transmission matrix is acquired using the Hadamard basis, the experimentally measured enhancement values closely match the theoretical upper limit expected in the absence of phase errors, given by:

$$\eta = \frac{\pi}{4}(N-1)+1.$$

This agreement demonstrates the effectiveness of the Hadamard-based dual-reference algorithm in maintaining high interferometric visibility and minimizing

measurement noise.

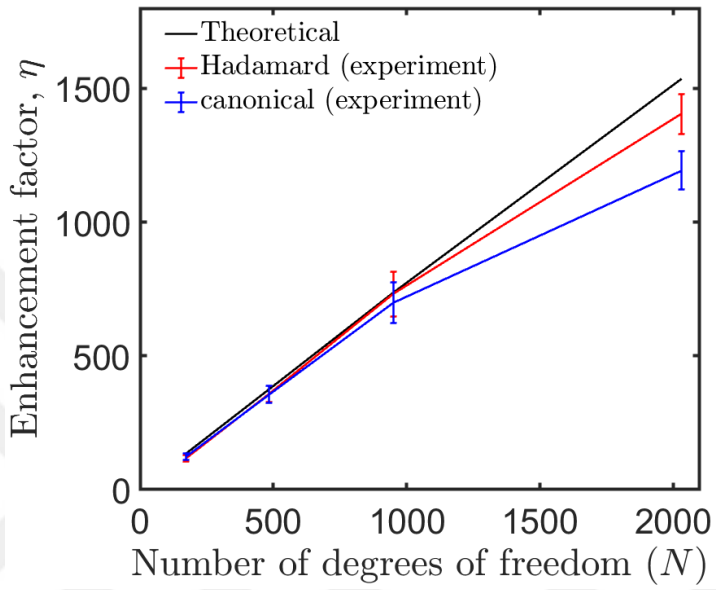

Figure 3.6: The mean enhancement factor η, averaged over the azimuthal angle θ and radial distances r at the fiber distal end, shown with respect to the number of degrees of freedom N = 172, 484, 952, and 2,032. The experimental enhancement factor η in the Hadamard basis (red solid line) closely follows the theoretical prediction (black solid line) and is notably higher than the experimental η in the canonical basis (blue solid line).

By contrast, for the same number of degrees of freedom (e.g., $N = 2000$), the enhancement obtained using the canonical basis underperforms relative to this theoretical benchmark. This discrepancy is attributed to a reduced signal-to-noise ratio that occurs at higher N, leading to increased phase retrieval errors and a corresponding degradation of focus intensity, captured by a phase error coefficient $\Phi < 1$.

To conclude our analysis of enhancement factor limitations arising from phase errors, Fig. 3.7 presents the measured enhancement values as a function of the number of controlled degrees of freedom N. These values are compared to theoretical expectations where the phase error coefficients Φ_m for both canonical and Hadamard basis measurements are taken into consideration.

The expected enhancement for phase-only modulation scales as $\eta = \frac{\pi}{4}\Phi(N -$

1) + 1, indicated by the solid lines. The experimental values (dashed lines with error bars) exhibit a systematic gap from the expected values, with the Hadamard basis consistently achieving higher values than the canonical basis across all N.

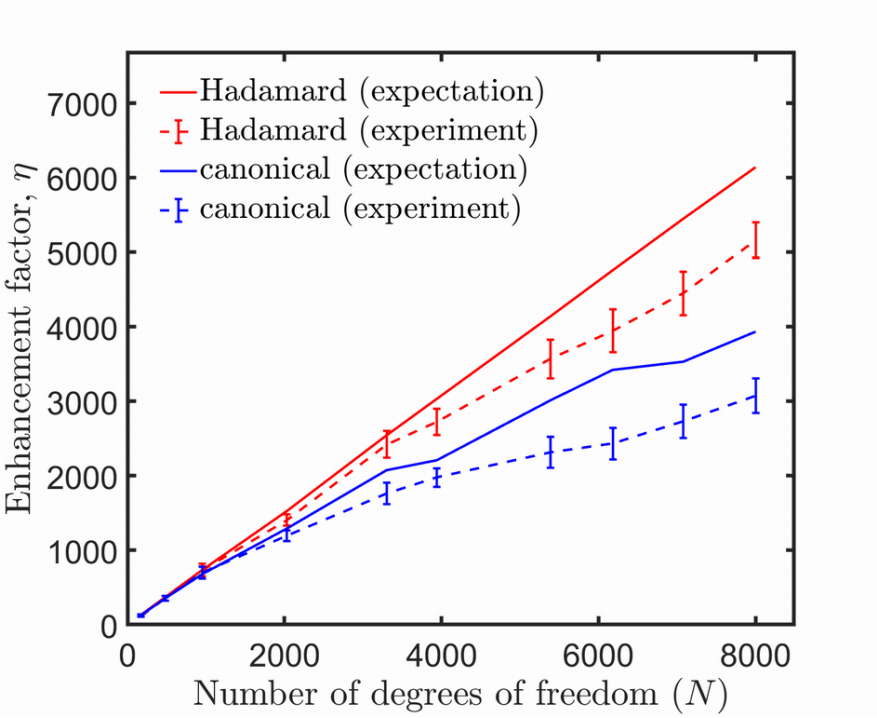

Figure 3.7: Enhancement factor η as a function of the number of controlled degrees of freedom N, for both canonical and Hadamard bases. Solid lines represent theoretical expectations based on experimentally measured phase error coefficients Φ for canonical and Hadamard TM measurements, while dashed lines with error bars denote experimental enhancement measurements. Both experimental enhancement factors from canonical and Hadamard TMs maintain close agreement with theoretical predictions up to $N = 3,000$. The enhancement for Hadamard-based TM measurements is consistently higher than the enhancement for canonical TM measurements. This result summarizes the influence of phase errors on the enhancement in wavefront shaping experiments through MMFs.

These deviations confirm that experimental imperfections, primarily phase errors, are the dominant factor limiting enhancement, even when the underlying theoretical bounds are preserved. Notably, the Hadamard basis demonstrates near-linear scaling with N, further validating its robustness to noise. In contrast, the canonical basis shows a slower growth in enhancement with increasing N, deviating from the linear trend. This deviation becomes more pronounced

at higher N and reflects the cumulative impact of phase errors on the canonical basis, consistent with our earlier analysis.

Taken together, these results demonstrate that although the theoretical limits of light focusing through multimode fibers are determined by the available degrees of freedom and the phase-only constraint, the practical performance is ultimately limited by phase errors. Understanding and mitigating these errors—particularly through an appropriate choice of basis—is essential for approaching the fundamental enhancement limits in wavefront shaping applications.

We also observe a systematic deviation between the experimental and theoretical enhancement values for $N > 3,000$. This discrepancy may stem from drifts in the experimental setup over long measurement durations, which can extend up to five hours.

Chapter 4

Optical Memory Effect with Focusing

The spatial memory effect enables computational imaging through complex media by exploiting inherent correlations in light propagation. In multimode fibers (MMFs), however, these spatial correlations are generally restricted to rotational memory effect, a consequence of their cylindrical symmetry. Furthermore, because the fiber length is much greater than its diameter, correlations along the radial direction are significantly diminished. In this chapter, we present an operator-based framework that addresses the limitations of conventional spatial correlations in MMFs. Specifically, we construct a novel operator that encodes radial memory effects, enabling controlled focusing under arbitrary radial displacements. Our method enables the integration of both radial and rotational memory effects in MMFs, allowing single-fiber imaging with a single wavefront correction applied at the proximal end.

4.1 Introduction to the Optical Memory Effect

The spatial memory effect is a fundamental speckle correlation phenomenon extensively utilized in computational imaging through highly scattering media such as biological tissue, fog, or scattering surfaces like white paint [107–110]. It refers to the persistence of spatial correlations in the speckle pattern at the output of a complex medium when the input wavefront undergoes small spatial or angular shifts [111–113]. In particular, the angular memory effect enables non-invasive imaging by allowing speckle scanning without loss of correlation in the speckle pattern, making it especially valuable in environments where conventional imaging is hindered by optical opacity [107–110]. Early demonstrations of imaging through opaque barriers leveraged phase retrieval techniques, such as Gerchberg–Saxton-type algorithms, to reconstruct images from intensity-only fluorescence measurements obtained in reflection [107]. Subsequent advancements enabled single-shot imaging from reflected light, significantly improving acquisition speed and broadening practical applicability [109].

When coherent light propagates through disordered or scattering media, its trajectory becomes highly sensitive to microscopic inhomogeneities, resulting in seemingly random interference patterns at the output. Despite this apparent randomness, the scattering process retains a degree of determinism: a small angular tilt of the input beam induces a measurable correlation between the output speckle patterns before and after the tilt [111,114,115]. This phenomenon, known as the angular memory effect, was first predicted theoretically by Feng et al. in 1988 and subsequently confirmed experimentally by Freund et al [111, 114]. The angular memory effect is generally observed in multiple-scattering media and is constrained by the physical thickness of the medium [111, 114].

As previously discussed, this effect has been instrumental in enabling non-invasive imaging through opaque layers, including the use of high-refractive-index scattering materials for high-resolution image reconstruction [108]. These techniques rely on the structural information encoded in speckle correlations. However, the imaging capability of the memory effect is fundamentally limited by its

finite angular range, which restricts the field of view (FoV). Importantly, the FoV narrows as the thickness of the scattering layer increases.

To address this limitation, operator-based approaches have been developed that extend the correlation range beyond the conventional angular memory effect range. These methods open the door for imaging through complex media at a wider field of view, effectively expanding the usable memory effect window [116]. A translational memory effect is naturally observed in structured waveguides such as square-core fibers [117] due to the broken rotational symmetry. In contrast, conventional step-index multimode fibers exhibit a rotational memory effect, consistent with their cylindrical symmetry, while correlation in the radial direction remains inherently limited [74, 118–120]. Here, we introduce a methodology that encodes radial correlations—i.e., the radial memory effect—through a multimode fiber, while simultaneously achieving a diffraction-limited focus that can be conveniently scanned along the radial direction by simply tilting or translating the incident wavefront at the fiber's proximal end. When combined with the rotational memory effect, our approach enables imaging through MMFs using a single incident wavefront.

4.2 Memory-Encoded Focusing Operator

To define the memory-encoded focusing operator, we exploit the fact that applying the complex conjugate of a specific row from the transmission matrix (TM) as the input field results in constructive interference at the corresponding output position on the CCD camera. Since each row of the TM represents the output field generated by a particular SLM input on a single CCD pixel, selecting a given row determines the input wavefront required to focus light at that pixel.

We first select the row associated with the target focal position and reshape it into a $L \times L$ dimensional array to match the spatial configuration of the input field on the spatial light modulator (SLM). Within this reshaped field, we define a region of interest (ROI), which is then reshaped back into a $1 \times L^2$ dimensional

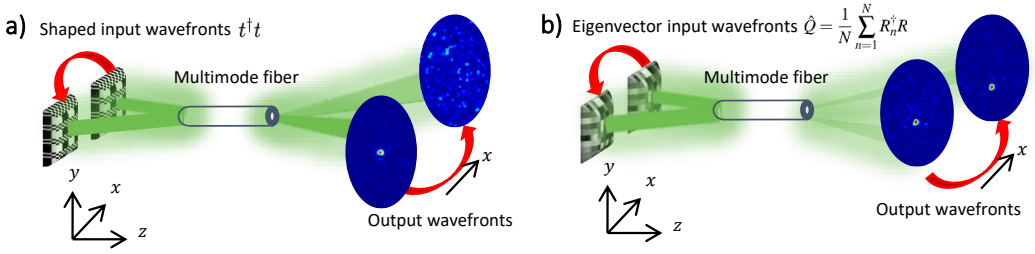

Figure 4.1: Operator-based wavefront shaping for focusing through a multimode fiber. (a) Shaped input wavefronts using the transmission matrix ($t^{\dagger}t$) enable focusing at the output facet, but the focus degrades under input translations due to the absence of radial memory effect. (b) Input wavefronts constructed from the eigenvectors of a memory-encoded focusing operator preserve the focus position even under input translations, demonstrating radial translational memory effect in the fiber.

vector, denoted as R_n.

We select a neighboring row (e.g., R_{n+1}) or a row corresponding to a more distant CCD pixel to realize a shift in the focal position at the output. This new row is similarly reshaped into two dimensions, and the ROI on the SLM is translated accordingly to reflect the desired shift at the input. The shifted ROI is then reshaped back into one dimension to obtain the modified input vector. This process effectively realizes an input field transformation that corresponds to an output focus shift.

Essentially, input shifts are implemented by reshaping each selected row of the transmission matrix into a two-dimensional input field on the SLM and translating the region of interest (ROI) on the SLM. The corresponding output shift is realized by selecting adjacent or distant rows, each of which corresponds to a different focus position on the CCD.

The memory-encoded focusing operator $\hat{Q}$, which has a dimension $L^2 \times L^2$, is then constructed as an average over the outer products of the reshaped input vectors, and is given by:

$$\hat{Q} = \frac{1}{N} \sum_{n=1}^{N} R_n^{\dagger} R_n \tag{4.1}$$

where R_n denotes the reshaped and shifted input vector corresponding to the n-th focus position.

4.2.1 Numerical Operator

To enable memory-encoded focusing through a multimode fiber (MMF), we construct an operator that explicitly encodes the radial memory effect using controlled input and output translations.

Starting from an experimentally measured transmission matrix t with $N = 740$ input degrees of freedom, we define the memory operator Q using eight selected row vectors R_n from t, where R_n corresponds to the field contribution for each SLM input on a specific output position on the CCD camera.

To implement controlled translations in the output plane, the distal end of a fiber with 50 µm core diameter is mapped onto a 540×540 output grid, so that each CCD camera pixel corresponds to 0.0926 µm in real space. Shifts are applied in integer pixel steps, with each step corresponding to a lateral displacement of 0.0926 µm per pixel. For visualization and normalization, these displacements are divided by the fiber radius, a = 25 µm, to yield the normalized shift r/a shown on the horizontal axis in Fig. 4.2, where each pixel step corresponds to $r/a = 0.0037$. For reference, a 2-pixel shift corresponds to $r/a = 0.0074$ (~ 0.185 µm), while a 7-pixel shift corresponds to $r/a = 0.0259$ (~ 0.648 µm) from the fiber center.

We use phase-only modulation in the simulations to match the experimental phase-only modulation. For single-point focusing with $N = 740$ input degrees of freedom, the theoretical maximum enhancement factor is given by $\eta = (\pi/4)(N - 1) + 1 = 581$ [42]. This expected value is consistent with the peak enhancement

observed in Fig. 4.2.

The eigenvectors of Q correspond to input fields that maintain high correlation with their output intensity profiles under radial translations, thereby encoding the memory effect within the focusing process. By transmitting the maximum eigenvector of Q through the MMF, we test its ability to produce a stable, high-intensity focus across a range of radial displacements without requiring recalibration for each new position.

Fig. 4.2 displays the intensity enhancement as a function of the normalized target output translation r/a. The memory-encoded focusing eigenvector input (red curve) maintains a significantly higher enhancement across a broader range of radial translations, while the conventional phase-conjugated input (blue curve) degrades rapidly.

The side panels illustrate the output intensity profiles for $r/a = 0$, 0.0074, and 0.0259, demonstrating that the memory-encoded focusing eigenvector preserves a focus under radial translation, whereas the conventional phase-conjugated input evolves into a speckle pattern. These results demonstrate that using eigenvectors of the memory-encoded focusing operator enables maintaining a stable focus under radial translations in MMFs without requiring recalculation of the input field for each shift and provide a basis for experimentally testing memory-encoded focusing in MMFs.

4.2.2 Experimental Operator

We experimentally implemented the memory-encoded focusing operator using the measured TM of our MMF system to demonstrate radial memory effect with focusing under controlled vertical translations of the input field on the SLM.

In our experiments, the number of input degrees of freedom used for wavefront shaping was $N = 256$, which, under ideal conditions, yields a theoretical single-point focusing enhancement of $\eta = (\pi/4)(N-1)+1 = 201$ for phase-only

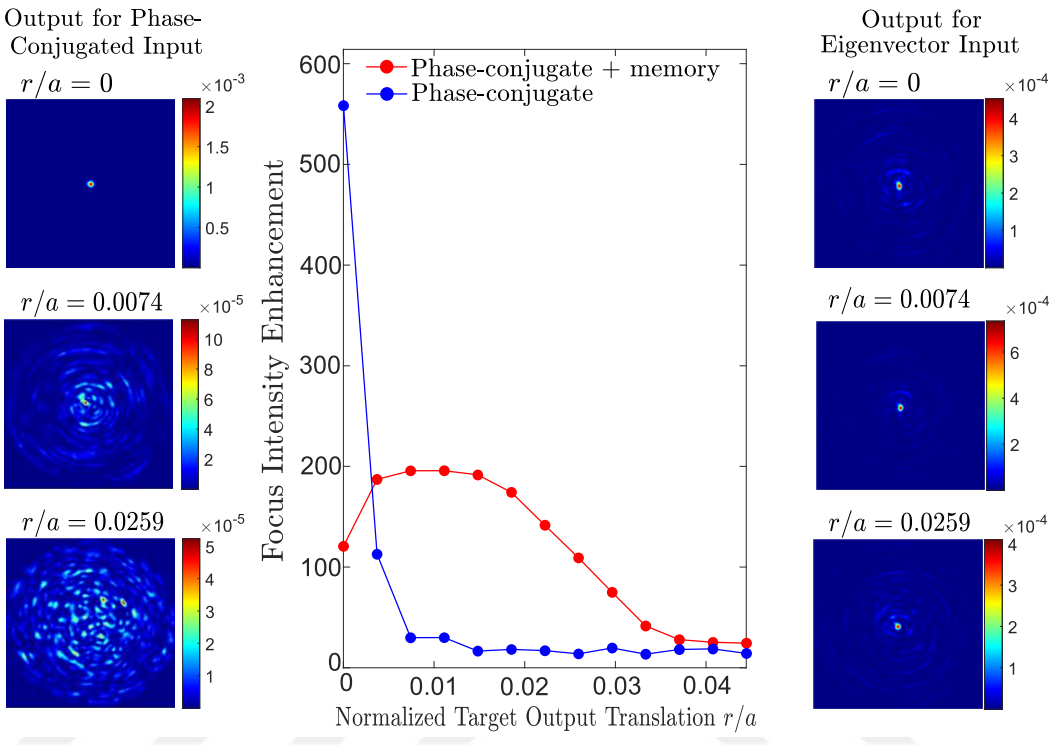

Figure 4.2: Numerical demonstration of memory-encoded focusing is shown. The central plot shows focus intensity enhancement versus normalized target output translation (r/a) for conventional phase-conjugated input (blue) and memory-encoded focusing eigenvector input (red). The memory-encoded focusing input maintains high enhancement across a broader range of radial shifts. Side panels display output intensity profiles at $r/a = 0$, 0.0074, and 0.0259, illustrating the degradation of the phase-conjugated focus with translation while the memory-encoded focus remains with radial translation.

modulation [42]. Since we performed phase-only modulation, only the phase of the memory-encoded focusing eigenvector was displayed on the SLM.

While the theoretical framework for single-point focusing enhancement is well-established, no model currently predicts enhancement factors for memory-encoded focusing in MMFs. In our experiments with the memory-encoded focusing eigenvector, the measured enhancement factors were $\eta^{(1)} = 61.39$ and $\eta^{(2)} = 62.45$. Using the multi-point focusing model with DOPC [121] as a reference, the expected enhancement η per focus is approximately $\eta = 100$.

We first examined the dual-point focusing scenario. The first case (Shift Index = 0) corresponds to zero input shift of the SLM segments, with transverse wavevector shifts $\Delta k_x^{(1)} = 0$ and $\Delta k_y^{(1)} = 0$. The output focus appeared at the center of the fiber facet, with $\Delta r^{(1)} = 0$ and $\Delta\theta^{(1)} = 0$, yielding a measured enhancement factor of $\eta^{(1)} = 61.39$.

In the second case (Shift index = 1), we applied a one-segment vertical translation to the input wavefront on the SLM, where each segment comprised 24×24 pixels. This introduced a shift of $\Delta k_x^{(2)} = 0$ and $\Delta k_y^{(2)} = 1$ segment, resulting in an output displacement of $\Delta r^{(2)} = 0.3704$ (corresponding to ~ 9.26 µm from the fiber center) while maintaining $\Delta\theta^{(2)} = 0$, with a measured enhancement factor of $\eta^{(2)} = 62.45$.

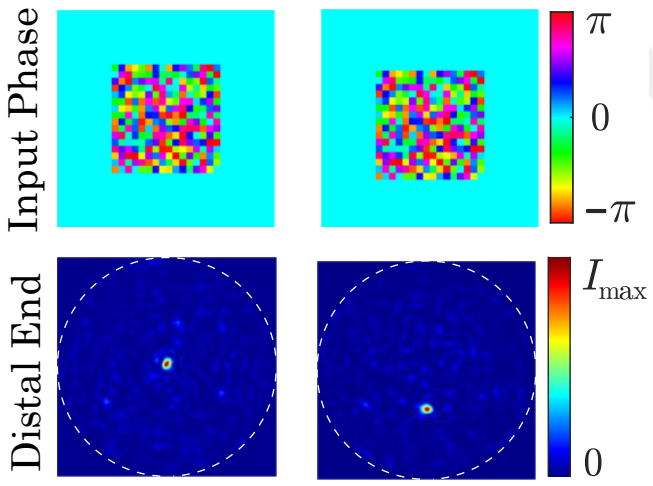

Figure 4.3: Experimental demonstration of dual-point focusing through the 50 µm MMF using the memory operator. **Left:** Input wavefront without radial translation (Shift index = 0) focuses at the center of the output facet with $\eta^{(1)} = 61.39$. **Right:** Input wavefront translated by one SLM segment along the vertical axis (Shift index = 1) shifts the output focus by $r/a = 0.3704$ (~ 9.26 µm from the fiber center) while maintaining high enhancement ($\eta^{(2)} = 62.45$).

Next, we demonstrated that a near-continuous radial shift of the focus can be achieved by constructing a memory-encoded focusing operator using four input-output rows of the transmission matrix, each corresponding to a different radial shift. Vertical shifts were applied to the input phase pattern on the SLM, using

$N = 256$ input segments, for the memory-encoded focusing eigenvector corresponding to the highest transmission eigenvalue. We tested four discrete input shifts and recorded the corresponding output displacements.

For the four tested cases (Shift Indices = 0, 1, 2, 3), the measured enhancement factors were $\eta^{(1)} = 47.57$, $\eta^{(2)} = 41.42$, $\eta^{(3)} = 26.03$, and $\eta^{(4)} = 24.67$, respectively. The output focus shifted to distinct radial positions at the distal end corresponding to each applied input shift. As shown in Fig. 4.4, the enhancement η decreased with increasing shift but remained significant, decreasing from ~ 48 to ~ 25 across the tested displacement range. These results demonstrate that memory-encoded focusing enables controlled multi-point focusing in MMFs under simple input wavefront translations without recalibration. This highlights the potential of this approach for single-fiber imaging and rapid scanning applications using a single optimized input pattern.

Given an ideal single-point enhancement of $\eta = 201$ under phase-only modulation, the expected enhancement for each focus in a four-point focusing configuration is approximately $\eta \approx 50$, as predicted by the theory of multi-point enhancement [121].

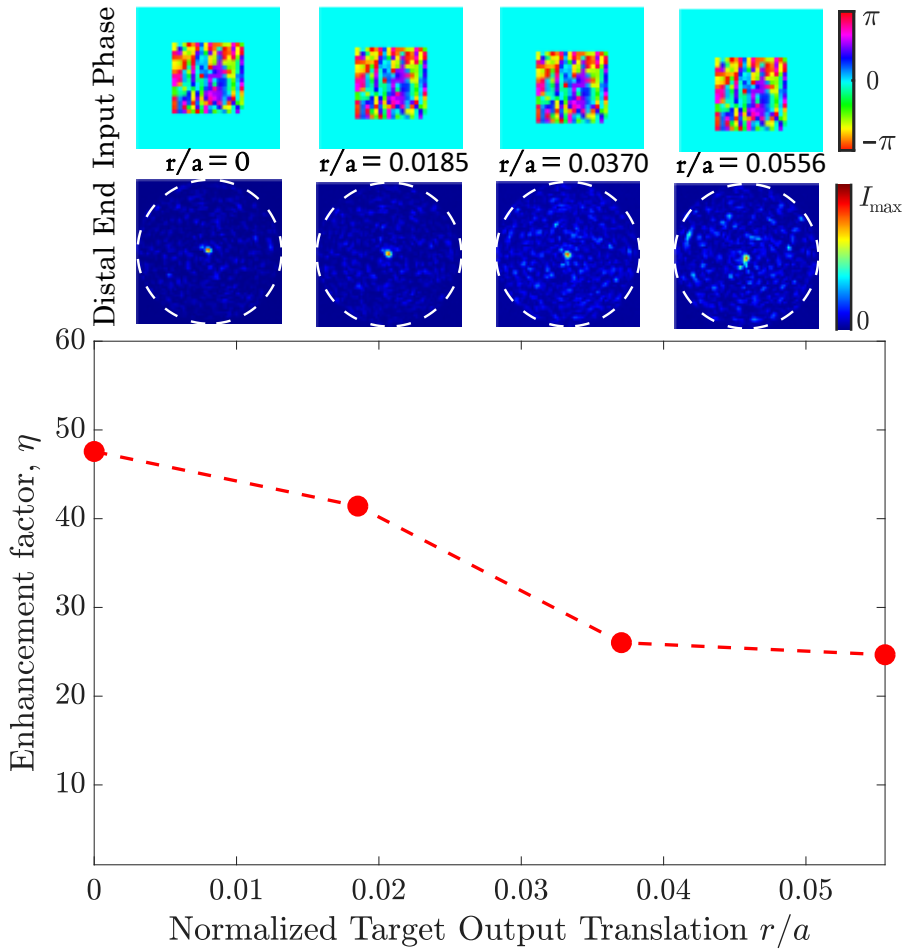

Figure 4.4: Experimental demonstration of multi-point focusing through the 50 µm-core-diameter MMF using the memory-encoded focusing operator. **Top:** Input phase patterns and corresponding distal end output intensity profiles for normalized output target shifts of $r/a = 0$ (0 µm), 0.0185 (0.463 µm), 0.0370 (0.926 µm), and 0.0556 (1.389 µm) from the fiber center. The input wavefronts are vertically translated on the SLM by 0, 1, 2, and 3 segments, respectively. **Bottom:** Measured enhancement factor η as a function of normalized target output translation r/a. The enhancement remains significant across all tested positions, decreasing from ~ 48 to ~ 25 as the output focus moves further from the center. These results demonstrate robust multi-point focusing enabled by the memory-encoded operator, maintaining high enhancement across multiple shifted target positions without recalibration.

Chapter 5

Conclusion & Future Work

This thesis has established a unified framework for understanding the limits of wavefront shaping through MMFs, particularly under experimental constraints. While MMFs offer a compact platform for high-resolution imaging, high-power light delivery, and optical communication, their complex modal structure imposes fundamental and practical limitations on light control. Addressing these limitations, this dissertation elucidates the fundamental conditions for optical focusing through multimode fibers using phase-only input modulation, bridging theoretical analysis, numerical simulations, and experimental observations.

Wavefront shaping in scattering media has been extensively studied, but similar rigorous analyses in MMFs are less common, and assumptions from scattering media are often applied without sufficient justification. Recognizing this gap, we aim to systematically understand which theoretical results from disordered systems carry over to MMFs and under what conditions, providing a clearer foundation for nearly precise light control through MMFs.

A central part of this work focuses on explaining why different wavefront shaping methods yield different enhancement factors in MMFs. A key finding is the demonstration that the dual reference algorithm provides higher enhancement,

due to its robustness against noise acquired during TM measurements. Importantly, we confirm that under phase-only input modulation in the Fourier domain, the participation ratio retains $R = \pi/4$, consistent with predictions from disordered scattering media. However, we emphasize that this correspondence holds only under specific experimental conditions, and MMFs cannot be treated as disordered systems without qualification.

Through detailed analyses of the experimental TMs, we further demonstrated how experimental parameters, such as SLM segment size, influence the effective TM rank and focusing performance. Such insights play a key role in advancing light control strategies that rely on the TM.

Moving beyond conventional focusing, we introduced an operator-based method for encoding the optical memory effect in the radial direction of the fiber. This approach enables scanning the focus along the radial direction by simply shifting the phase pattern -corresponding to the dominant eigenvector of a memory-encoded focusing operator- on the SLM. This allows scanning the focus at the output with simple transformations such as tilting and shifting of the input field pattern.

Looking ahead, the integration of radial and rotational memory effects could enable two-dimensional scanning at the fiber's distal end, which is a key step toward fully programmable fiber imaging systems. In parallel, implementing memory-effect-based focusing using reflection-only measurements could eliminate the need for distal access, making the method more viable for practical applications.

In summary, this work closes critical gaps between theoretical wavefront shaping limits and real-world fiber implementations. It not only explains the origin of performance limitations but also introduces new strategies to overcome them. These results have direct relevance for high-resolution fiber imaging, compact beam delivery systems, and advanced photonic architectures requiring precise light control through complex media.

Bibliography

[1] T. Čižmár and K. Dholakia, "Exploiting multimode waveguides for pure fibre-based imaging," *Nat. Commun.*, vol. 3, p. 1027, 2012.

[2] Y. Choi, C. Yoon, M. Kim, T. D. Yang, C. Fang-Yen, R. R. Dasari, K. J. Lee, and W. Choi, "Scanner-free and wide-field endoscopic imaging by using a single multimode optical fiber," *Physical review letters*, vol. 109, no. 20, p. 203901, 2012.

[3] I. N. Papadopoulos, S. Farahi, C. Moser, and D. Psaltis, "Focusing and scanning light through a multimode optical fiber using digital phase conjugation," *Optics express*, vol. 20, no. 10, pp. 10583–10590, 2012.

[4] I. N. Papadopoulos, S. Farahi, C. Moser, and D. Psaltis, "High-resolution, lensless endoscope based on digital scanning through a multimode optical fiber," *Biomedical optics express*, vol. 4, no. 2, pp. 260–270, 2013.

[5] D. Loterie, S. Farahi, I. Papadopoulos, A. Goy, D. Psaltis, and C. Moser, "Digital confocal microscopy through a multimode fiber," *Opt. Express*, vol. 23, no. 18, pp. 23845–23858, 2015.

[6] L. V. Amitonova and J. F. De Boer, "Compressive imaging through a multimode fiber," *Opt. Lett.*, vol. 43, no. 21, pp. 5427–5430, 2018.

[7] L. V. Amitonova and J. F. de Boer, "Endo-microscopy beyond the abbe and nyquist limits," *Light: Science & Applications*, vol. 9, no. 1, p. 81, 2020.

[8] S. A. Vasquez-Lopez, R. Turcotte, V. Koren, M. Plöschner, Z. Padamsey, M. J. Booth, T. Čižmár, and N. J. Emptage, "Subcellular spatial resolution achieved for deep-brain imaging in vivo using a minimally invasive multimode fiber," *Light: science & applications*, vol. 7, no. 1, p. 110, 2018.

[9] T. Čižmár and K. Dholakia, "Shaping the light transmission through a multimode optical fibre: complex transformation analysis and applications in biophotonics," *Optics express*, vol. 19, no. 20, pp. 18871–18884, 2011.

[10] I. T. Leite, S. Turtaev, X. Jiang, M. Šiler, A. Cuschieri, P. S. J. Russell, and T. Čižmár, "Three-dimensional holographic optical manipulation through a high-numerical-aperture soft-glass multimode fibre," *Nature Photonics*, vol. 12, no. 1, pp. 33–39, 2018.

[11] K. Li, X. Chen, A. R. Zakharian, J. E. Hurley, J. S. Stone, and M.-J. Li, "Large core multimode fiber with high bandwidth and high connector tolerance for broadband short distance communications," *APL Photonics*, vol. 6, no. 7, 2021.

[12] E. Kakkava, M. Romito, D. B. Conkey, D. Loterie, K. M. Stankovic, C. Moser, and D. Psaltis, "Selective femtosecond laser ablation via two-photon fluorescence imaging through a multimode fiber," *Biomedical optics express*, vol. 10, no. 2, pp. 423–433, 2019.

[13] B. Redding and H. Cao, "Using a multimode fiber as a high-resolution,<? a3b2 show [pmg: line-break justify=" yes"/]?> low-loss spectrometer," *Optics letters*, vol. 37, no. 16, pp. 3384–3386, 2012.

[14] B. Redding, S. M. Popoff, and H. Cao, "All-fiber spectrometer based on speckle pattern reconstruction," *Optics express*, vol. 21, no. 5, pp. 6584–6600, 2013.

[15] H. Cao, "Perspective on speckle spectrometers," *J. Opt*, vol. 19, no. 6, p. 060402, 2017.

[16] J. W. Dawson, M. J. Messerly, R. J. Beach, M. Y. Shverdin, E. A. Stappaerts, A. K. Sridharan, P. H. Pax, J. E. Heebner, C. W. Siders, and

C. Barty, "Analysis of the scalability of diffraction-limited fiber lasers and amplifiers to high average power," *Optics express*, vol. 16, no. 17, pp. 13240–13266, 2008.

[17] D. J. Richardson, J. Nilsson, and W. A. Clarkson, "High power fiber lasers: current status and future perspectives," *Journal of the optical society of America B*, vol. 27, no. 11, pp. B63–B92, 2010.

[18] M. N. Zervas and C. A. Codemard, "High power fiber lasers: a review," *IEEE Journal of selected topics in Quantum Electronics*, vol. 20, no. 5, pp. 219–241, 2014.

[19] S. Fu, W. Shi, Y. Feng, L. Zhang, Z. Yang, S. Xu, X. Zhu, R. A. Norwood, and N. Peyghambarian, "Review of recent progress on single-frequency fiber lasers," *Journal of the Optical Society of America B*, vol. 34, no. 3, pp. A49–A57, 2017.

[20] S. Rothe, K. Wisal, C.-W. Chen, M. Ercan, A. Jesacher, A. D. Stone, and H. Cao, "Output beam shaping of a multimode fiber amplifier," *Optics Communications*, vol. 577, p. 131405, 2025.

[21] S. Rothe, C.-W. CHen, P. Ahmadi, K. Wisal, M. Ercan, K. Lee, N. VIgne, A. D. Stone, and H. Cao, "Wavefront shaping enables high-power multimode fiber amplifier with output control," *arXiv preprint arXiv:2504.06423*, 2025.

[22] R. Florentin, V. Kermene, J. Benoist, A. Desfarges-Berthelemot, D. Pagnoux, A. Barthélémy, and J.-P. Huignard, "Shaping the light amplified in a multimode fiber," *Light: Science & Applications*, vol. 6, no. 2, pp. e16208–e16208, 2017.

[23] E. Marcatili, "Modal dispersion in optical fibers with arbitrary numerical aperture and profile dispersion," *The Bell System Technical Journal*, vol. 56, no. 1, pp. 49–63, 1977.

[24] C. Antonelli, A. Mecozzi, M. Shtaif, and P. J. Winzer, "Stokes-space analysis of modal dispersion in fibers with multiple mode transmission," *Optics express*, vol. 20, no. 11, pp. 11718–11733, 2012.

[25] L. B. Soldano and E. C. Pennings, "Optical multi-mode interference devices based on self-imaging: principles and applications," *Journal of lightwave technology*, vol. 13, no. 4, pp. 615–627, 1995.

[26] I. Turek, I. Martincek, and R. Stransky, "Interference of modes in optical fibers," *Optical Engineering*, vol. 39, no. 5, pp. 1304–1309, 2000.

[27] A. Garito, J. Wang, and R. Gao, "Effects of random perturbations in plastic optical fibers," *Science*, vol. 281, no. 5379, pp. 962–967, 1998.

[28] R. Di Leonardo and S. Bianchi, "Hologram transmission through multi-mode optical fibers," *Opt. Express*, vol. 19, no. 1, pp. 247–254, 2011.

[29] A. P. Mosk, A. Lagendijk, G. Lerosey, and M. Fink, "Controlling waves in space and time for imaging and focusing in complex media," *Nat. Photonics*, vol. 6, no. 5, p. 283, 2012.

[30] R. Horstmeyer, H. Ruan, and C. Yang, "Guidestar-assisted wavefront-shaping methods for focusing light into biological tissue," *Nat. Photonics*, vol. 9, no. 9, pp. 563–571, 2015.

[31] I. M. Vellekoop, "Feedback-based wavefront shaping," *Opt. Express*, vol. 23, no. 9, pp. 12189–12206, 2015.

[32] S. Rotter and S. Gigan, "Light fields in complex media: mesoscopic scattering meets wave control," *Rev. Mod. Phys.*, vol. 89, p. 015005, 2017.

[33] O. Tzang, A. M. Caravaca-Aguirre, K. Wagner, and R. Piestun, "Adaptive wavefront shaping for controlling nonlinear multimode interactions in optical fibres," *Nature Photonics*, vol. 12, no. 6, pp. 368–374, 2018.

[34] S. Gigan, O. Katz, H. B. De Aguiar, E. R. Andresen, A. Aubry, J. Bertolotti, E. Bossy, D. Bouchet, J. Brake, S. Brasselet, *et al.*, "Roadmap on wavefront shaping and deep imaging in complex media," *J. Phys. Photonics*, vol. 4, no. 4, p. 042501, 2022.

[35] H. Cao, A. P. Mosk, and S. Rotter, "Shaping the propagation of light in complex media," *Nature Physics*, vol. 18, no. 9, pp. 994–1007, 2022.

[36] H. Cao, T. Čižmár, S. Turtaev, T. Tyc, and S. Rotter, "Controlling light propagation in multimode fibers for imaging, spectroscopy, and beyond," *Adv. Opt. Photonics*, vol. 15, no. 2, pp. 524–612, 2023.

[37] C.-W. Chen, L. V. Nguyen, K. Wisal, S. Wei, S. C. Warren-Smith, O. Henderson-Sapir, E. P. Schartner, P. Ahmadi, H. Ebendorff-Heidepriem, A. D. Stone, D. J. Ottaway, and H. Cao, "Mitigating stimulated brillouin scattering in multimode fibers with focused output via wavefront shaping," *Nat. Commun.*, vol. 14, Nov. 2023.

[38] K. Wisal, C.-W. Chen, Z. Kuang, O. D. Miller, H. Cao, and A. D. Stone, "Optimal input excitations for suppressing nonlinear instabilities in multimode fibers," *Optica*, vol. 11, no. 12, pp. 1663–1672, 2024.

[39] A. M. Paniagua-Diaz, W. L. Barnes, and J. Bertolotti, "Wavefront shaping to improve beam quality: converting a speckle pattern into a gaussian spot," *Physica Scripta*, vol. 98, no. 3, p. 035516, 2023.

[40] Y. Xu, K. Zheng, J. Shang, W. Yuan, S. Fu, H. Lu, Y. Wang, and Y. Qin, "Wavefront shaping for reconfigurable beam steering in lithium niobate multimode waveguide," *Optics Letters*, vol. 47, no. 2, pp. 329–332, 2022.

[41] L. Collard, F. Pisano, M. Pisanello, A. Balena, M. De Vittorio, and F. Pisanello, "Wavefront engineering for controlled structuring of far-field intensity and phase patterns from multimodal optical fibers," *APL Photonics*, vol. 6, no. 5, 2021.

[42] I. M. Vellekoop and A. P. Mosk, "Focusing coherent light through opaque strongly scattering media," *Opt. Lett.*, vol. 32, no. 16, pp. 2309–2311, 2007.

[43] S. M. Popoff, G. Lerosey, R. Carminati, M. Fink, A. C. Boccara, and S. Gigan, "Measuring the transmission matrix in optics: an approach to the study and control of light propagation in disordered media," *Phys. Rev. Lett.*, vol. 104, p. 100601, 2010.

[44] S. Popoff, G. Lerosey, M. Fink, A. C. Boccara, and S. Gigan, "Image transmission through an opaque material," *Nature communications*, vol. 1, no. 1, p. 81, 2010.

[45] M. Kim, W. Choi, Y. Choi, C. Yoon, and W. Choi, "Transmission matrix of a scattering medium and its applications in biophotonics," *Opt. Express*, vol. 23, pp. 12648–12668, 2015.

[46] N. Bender, H. Haig, D. N. Christodoulides, and F. W. Wise, "Spectral speckle customization," *Optica*, vol. 10, no. 10, pp. 1260–1268, 2023.

[47] C. Stockbridge, Y. Lu, J. Moore, S. Hoffman, R. Paxman, K. Toussaint, and T. Bifano, "Focusing through dynamic scattering media," *Optics express*, vol. 20, no. 14, pp. 15086–15092, 2012.

[48] I. M. Vellekoop, A. Lagendijk, and A. Mosk, "Exploiting disorder for perfect focusing," *Nat. Photonics*, vol. 4, no. 5, pp. 320–322, 2010.

[49] A. M. Caravaca-Aguirre, E. Niv, D. B. Conkey, and R. Piestun, "Real-time resilient focusing through a bending multimode fiber," *Opt. Express*, vol. 21, pp. 12881–12887, 2013.

[50] L. V. Amitonova, A. Descloux, J. Petschulat, M. H. Frosz, G. Ahmed, F. Babic, X. Jiang, A. P. Mosk, P. S. Russell, and P. W. H. Pinkse, "High-resolution wavefront shaping with a photonic crystal fiber for multimode fiber imaging," *Opt. Lett.*, vol. 41, pp. 497–500, 2016.

[51] A. Descloux, L. V. Amitonova, and P. W. H. Pinkse, "Aberrations of the point spread function of a multimode fiber due to partial mode excitation," *Opt. Express*, vol. 24, pp. 18501–18512, 2016.

[52] Z. Lyu, G. Osnabrugge, P. W. H. Pinkse, and L. V. Amitonova, "Focus quality in raster-scan imaging via a multimode fiber," *Appl. Opt.*, vol. 61, pp. 4363–4369, 2022.

[53] A. D. Gomes, S. Turtaev, Y. Du, and T. Čižmár, "Near perfect focusing through multimode fibres," *Opt. Express*, vol. 30, no. 7, pp. 10645–10663, 2022.

[54] Z. Lyu and L. V. Amitonova, "Wavefront shaping and imaging through a multimode hollow-core fiber," *Optics Express*, vol. 32, no. 21, pp. 37098–37107, 2024.

[55] S. Resisi, Y. Viernik, S. M. Popoff, and Y. Bromberg, "Wavefront shaping in multimode fibers by transmission matrix engineering," *APL Photonics*, vol. 5, no. 3, 2020.

[56] B. Mastiani, D. Cox, and I. M. Vellekoop, "Practical considerations for high-fidelity wavefront shaping experiments," *J. Phys. Photonics*, vol. 6, no. 3, p. 033003, 2024.

[57] D. Psaltis and C. Moser, "Imaging with multimode fibers," *Optics and Photonics News*, vol. 27, no. 1, pp. 24–31, 2016.

[58] S. Yoon, M. Kim, M. Jang, Y. Choi, W. Choi, S. Kang, and W. Choi, "Deep optical imaging within complex scattering media," *Nature Reviews Physics*, vol. 2, no. 3, pp. 141–158, 2020.

[59] S. Gigan, "Optical microscopy aims deep," *Nature Photonics*, vol. 11, no. 1, pp. 14–16, 2017.

[60] S. Leedumrongwatthanakun, L. Innocenti, H. Defienne, T. Juffmann, A. Ferraro, M. Paternostro, and S. Gigan, "Programmable linear quantum networks with a multimode fibre," *Nature Photonics*, vol. 14, no. 3, pp. 139–142, 2020.

[61] S.-Y. Lee, "MMF-simulation." `https://github.com/szuyul/MMF-simulation/releases/tag/v1.0`, 2023.

[62] A. W. Snyder, J. D. Love, *et al.*, *Optical waveguide theory*, vol. 175. Chapman and hall London, 1983.

[63] A. K. Ghatak and K. Thyagarajan, *An introduction to fiber optics*. Cambridge university press, 1998.

[64] K. Okamoto, *Fundamentals of optical waveguides*. Elsevier, 2021.

[65] K. Iizuka, *Elements of Photonics, Volume I: In Free Space and Special Media*, vol. 1. John Wiley & Sons, 2002.

[66] M. Plöschner, T. Tyc, and T. Čižmár, "Seeing through chaos in multimode fibres," *Nat. Photonics*, vol. 9, pp. 529–535, 2015.

[67] A. Snyder, "Coupled-mode theory for optical fibers," *Journal of the Optical Society of America*, vol. 62, pp. 1267–1277, 1972.

[68] W. Xiong, P. Ambichl, Y. Bromberg, B. Redding, S. Rotter, and H. Cao, "Spatiotemporal control of light transmission through a multimode fiber with strong mode coupling," *Physical review letters*, vol. 117, no. 5, p. 053901, 2016.

[69] H. Defienne and D. Faccio, "Arbitrary spatial mode sorting in a multimode fiber," *Physical Review A*, vol. 101, no. 6, p. 063830, 2020.

[70] G. Pelc, S. Guterman, R. Gutiérrez-Cuevas, A. Goetschy, S. M. Popoff, and Y. Bromberg, "Open transmission channels in multimode fiber cavities with random mode mixing," *arXiv preprint arXiv:2502.01596*, 2025.

[71] M. Fink, D. Cassereau, A. Derode, C. Prada, P. Roux, M. Tanter, J.-L. Thomas, and F. Wu, "Time-reversed acoustics," *Reports on progress in Physics*, vol. 63, no. 12, p. 1933, 2000.

[72] G. Lerosey, J. de Rosny, A. Tourin, A. Derode, G. Montaldo, and M. Fink, "Time reversal of electromagnetic waves," *Physical review letters*, vol. 92, no. 19, p. 193904, 2004.

[73] B. Mastiani, G. Osnabrugge, and I. M. Vellekoop, "Wavefront shaping for forward scattering," *Optics express*, vol. 30, no. 21, pp. 37436–37445, 2022.

[74] S. Li, S. A. R. Horsley, T. Tyc, T. Čižmár, and D. B. Phillips, "Memory effect assisted imaging through multimode optical fibres," *Nat. Commun.*, vol. 12, p. 3751, 2021.

[75] I. M. Vellekoop and A. P. Mosk, "Universal optimal transmission of light through disordered materials," *Phys. Rev. Lett.*, vol. 101, p. 120601, 2008.

[76] I. M. Vellekoop and A. Mosk, "Phase control algorithms for focusing light through turbid media," *Opt. Commun.*, vol. 281, no. 11, pp. 3071–3080, 2008.

[77] I. M. Vellekoop and C. Aegerter, "Scattered light fluorescence microscopy: imaging through turbid layers," *Opt. Lett.*, vol. 35, pp. 1245—1247, 2010.

[78] J. Xu, H. Ruan, Y. Liu, H. Zhou, and C. Yang, "Focusing light through scattering media by transmission matrix inversion," *Optics express*, vol. 25, no. 22, pp. 27234–27246, 2017.

[79] R. Y. Gu, R. N. Mahalati, and J. M. Kahn, "Design of flexible multi-mode fiber endoscope," *Optics express*, vol. 23, no. 21, pp. 26905–26918, 2015.

[80] D. Loterie, D. Psaltis, and C. Moser, "Bend translation in multimode fiber imaging," *Optics express*, vol. 25, no. 6, pp. 6263–6273, 2017.

[81] A. Drémeau, A. Liutkus, D. Martina, O. Katz, C. Schülke, F. Krzakala, S. Gigan, and L. Daudet, "Reference-less measurement of the transmission matrix of a highly scattering material using a dmd and phase retrieval techniques," *Optics express*, vol. 23, no. 9, pp. 11898–11911, 2015.

[82] D. Wang, E. H. Zhou, J. Brake, H. Ruan, M. Jang, and C. Yang, "Focusing through dynamic tissue with millisecond digital optical phase conjugation," *Optica*, vol. 2, no. 8, pp. 728–735, 2015.

[83] Y. Liu, C. Ma, Y. Shen, J. Shi, and L. V. Wang, "Focusing light inside dynamic scattering media with millisecond digital optical phase conjugation," *Optica*, vol. 4, no. 2, pp. 280–288, 2017.

[84] Y. Shen, Y. Liu, C. Ma, and L. V. Wang, "Focusing light through scattering media by full-polarization digital optical phase conjugation," *Optics letters*, vol. 41, no. 6, pp. 1130–1133, 2016.

[85] H. Yılmaz, W. L. Vos, and A. P. Mosk, "Optimal control of light propagation through multiple-scattering media in the presence of noise," *Biomed. Opt. Express*, vol. 4, pp. 1759–1768, 2013.

[86] B. Mastiani and I. M. Vellekoop, "Noise-tolerant wavefront shaping in a hadamard basis," *Opt. Express*, vol. 29, no. 11, pp. 17534–17541, 2021.

[87] K. Wisal, S. C. Warren-Smith, C.-W. Chen, H. Cao, and A. D. Stone, "Theory of stimulated brillouin scattering in fibers for highly multimode excitations," *Physical Review X*, vol. 14, no. 3, p. 031053, 2024.

[88] F. van Beijnum, "Light takes no shortcuts," Master's thesis, University of Twente, 2009.

[89] H. Yılmaz, C. W. Hsu, A. Yamilov, and H. Cao, "Transverse localization of transmission eigenchannels," *Nat. Photonics*, vol. 13, pp. 352–358, 2019.

[90] H. Yılmaz, C. W. Hsu, A. Goetschy, S. Bittner, S. Rotter, A. Yamilov, and H. Cao, "Angular memory effect of transmission eigenchannels," *Phys. Rev. Lett.*, vol. 123, p. 203901, Nov 2019.

[91] J. H. Bruning, D. R. Herriott, J. E. Gallagher, D. P. Rosenfeld, A. D. White, and D. J. Brangaccio, "Digital wavefront measuring interferometer for testing optical surfaces and lenses," *Applied optics*, vol. 13, no. 11, pp. 2693–2703, 1974.

[92] J. Schwider, R. Burow, K.-E. Elssner, J. Grzanna, R. Spolaczyk, and K. Merkel, "Digital wave-front measuring interferometry: some systematic error sources," *Applied optics*, vol. 22, no. 21, pp. 3421–3432, 1983.

[93] D. W. Cox and I. M. Vellekoop, "Orthonormalization of phase-only basis functions," *Optics express*, vol. 33, no. 2, pp. 2427–2436, 2025.

[94] X. Tao, T. Lam, B. Zhu, Q. Li, M. R. Reinig, and J. Kubby, "Three-dimensional focusing through scattering media using conjugate adaptive optics with remote focusing (caorf)," *Optics express*, vol. 25, no. 9, pp. 10368–10383, 2017.

[95] C. L. Lawson and R. J. Hanson, *Solving least squares problems*. SIAM, 1995.

[96] G. W. Stewart, "On the perturbation of pseudo-inverses, projections and linear least squares problems," *SIAM review*, vol. 19, no. 4, pp. 634–662, 1977.

[97] W. Choi, A. P. Mosk, Q.-H. Park, and W. Choi, "Transmission eigenchannels in a disordered medium," *Physical Review B—Condensed Matter and Materials Physics*, vol. 83, no. 13, p. 134207, 2011.

[98] M. Kim, Y. Choi, C. Yoon, W. Choi, J. Kim, Q.-H. Park, and W. Choi, "Maximal energy transport through disordered media with the implementation of transmission eigenchannels," *Nature photonics*, vol. 6, no. 9, pp. 581–585, 2012.

[99] C. W. Hsu, S. F. Liew, A. Goetschy, H. Cao, and A. Douglas Stone, "Correlation-enhanced control of wave focusing in disordered media," *Nature Physics*, vol. 13, no. 5, pp. 497–502, 2017.

[100] R. Sarma, A. G. Yamilov, S. Petrenko, Y. Bromberg, and H. Cao, "Control of energy density inside a disordered medium by coupling to open or closed channels," *Physical review letters*, vol. 117, no. 8, p. 086803, 2016.

[101] A. Ammar, S. F. Şener, M. Ercan, and H. Yılmaz, "Upper bounds of focusing light through multimode fibers," *arXiv preprint arXiv:2504.07626*, 2025.

[102] M. Duan, Y. Zhao, Z. Yang, X. Deng, H. Huangfu, H. Zuo, Z. Li, and D. Wang, "Modulate scattered light field with point guard algorithm," *Opt. Commun.*, vol. 548, p. 129832, 2023.

[103] S. Resisi, Y. Viernik, S. M. Popoff, and Y. Bromberg, "Wavefront shaping in multimode fibers by transmission matrix engineering," *APL Photonics*, vol. 5, p. 036103, 2020.

[104] W. Xiong, C. W. Hsu, Y. Bromberg, J. E. Antonio-Lopez, R. Amezcua Correa, and H. Cao, "Complete polarization control in multimode fibers with polarization and mode coupling," *Light: Science & Applications*, vol. 7, no. 1, p. 54, 2018.

[105] H. B. de Aguiar, S. Gigan, and S. Brasselet, "Polarization recovery through scattering media," *Science Advances*, vol. 3, no. 9, p. e1600743, 2017.

[106] M. Jang, C. Yang, and I. Vellekoop, "Optical phase conjugation with less than a photon per degree of freedom," *Phys. Rev. Lett.*, vol. 118, no. 9, p. 093902, 2017.

[107] J. Bertolotti, E. G. Van Putten, C. Blum, A. Lagendijk, W. L. Vos, and A. P. Mosk, "Non-invasive imaging through opaque scattering layers," *Nature*, vol. 491, no. 7423, pp. 232–234, 2012.

[108] H. Yilmaz, E. G. van Putten, J. Bertolotti, A. Lagendijk, W. L. Vos, and A. P. Mosk, "Speckle correlation resolution enhancement of wide-field fluorescence imaging," *Optica*, vol. 2, no. 5, pp. 424–429, 2015.

[109] O. Katz, P. Heidmann, M. Fink, and S. Gigan, "Non-invasive single-shot imaging through scattering layers and around corners via speckle correlations," *Nature photonics*, vol. 8, no. 10, pp. 784–790, 2014.

[110] X. Yang, Y. Pu, and D. Psaltis, "Imaging blood cells through scattering biological tissue using speckle scanning microscopy," *Optics express*, vol. 22, no. 3, pp. 3405–3413, 2014.

[111] I. Freund, M. Rosenbluh, and S. Feng, "Memory effects in propagation of optical waves through disordered media," *Physical review letters*, vol. 61, no. 20, p. 2328, 1988.

[112] R. Berkovits and S. Feng, "Correlations in coherent multiple scattering," *Physics Reports*, vol. 238, no. 3, pp. 135–172, 1994.

[113] B. Judkewitz, R. Horstmeyer, I. M. Vellekoop, I. N. Papadopoulos, and C. Yang, "Translation correlations in anisotropically scattering media," *Nature physics*, vol. 11, no. 8, pp. 684–689, 2015.

[114] S. Feng, C. Kane, P. A. Lee, and A. D. Stone, "Correlations and fluctuations of coherent wave transmission through disordered media," *Physical review letters*, vol. 61, no. 7, p. 834, 1988.

[115] G. Osnabrugge, R. Horstmeyer, I. N. Papadopoulos, B. Judkewitz, and I. M. Vellekoop, "Generalized optical memory effect," *Optica*, vol. 4, no. 8, pp. 886–892, 2017.

[116] H. Yılmaz, M. Kühmayer, C. W. Hsu, S. Rotter, and H. Cao, "Customizing the angular memory effect for scattering media," *Physical Review X*, vol. 11, no. 3, p. 031010, 2021.

[117] S. Mezil, I. Wang, and E. Bossy, "Imaging through a square multimode fiber by scanning focused spots with the memory effect," *Optics Letters*, vol. 48, no. 17, pp. 4701–4704, 2023.

[118] D. Bouchet, A. M. Caravaca-Aguirre, G. Godefroy, P. Moreau, I. Wang, and E. Bossy, "Speckle-correlation imaging through a kaleidoscopic multimode fiber," *Proceedings of the National Academy of Sciences*, vol. 120, no. 26, p. e2221407120, 2023.

[119] A. M. Caravaca-Aguirre, A. Carron, S. Mezil, I. Wang, and E. Bossy, "Optical memory effect in square multimode fibers," *Optics Letters*, vol. 46, no. 19, pp. 4924–4927, 2021.

[120] L. V. Amitonova, A. P. Mosk, and P. W. Pinkse, "Rotational memory effect of a multimode fiber," *Optics express*, vol. 23, no. 16, pp. 20569–20575, 2015.

[121] I. M. Vellekoop, E. Van Putten, A. Lagendijk, and A. Mosk, "Demixing light paths inside disordered metamaterials," *Optics express*, vol. 16, no. 1, pp. 67–80, 2008.